Detailed theoretical and experimental analysis of low-energy electron-N_2 scattering

Weiguo Sun,[1,*] Michael A. Morrison,[1] William A. Isaacs,[1] Wayne K. Trail,[1] Dean T. Alle,[2] R. J. Gulley,[2] Michael J. Brennan,[2] and Stephen J. Buckman[2]

[1]*Department of Physics & Astronomy, University of Oklahoma, Norman, Oklahoma 73019-0225*

[2]*Research School of Physical Sciences and Engineering, Australian National University, Canberra, Australian Capital Territory, Australia*

(Received 11 January 1995)

We have carried out a comprehensive theoretical and experimental study of electron scattering from molecular nitrogen at energies below 10.0 eV. In the theoretical component of this project we have generated differential and integral cross sections for elastic scattering and vibrational excitation in converged vibrational close-coupling calculations. In the experiments, we have measured differential cross sections for these processes at scattering angles from 20° to 130° in a crossed-beam experiment at a large number of energies between 0.55 and 10 eV and, in a complementary time-of-flight experiment, total cross sections at energies between 0.08 and 10.0 eV. The measured angular distributions have been extrapolated to 0° and 180° using a procedure based on a nonlinear least-squares fit constrained by known physical properties of the e-N_2 scattering matrix; numerical integration of the resulting extrapolated distributions yields integrated cross sections with almost no error beyond that inherent in the measured angular data. We find generally good agreement between the present experimental and theoretical cross section, particularly at energies near the Π_g resonance near 2.39 eV. In previous studies of scattering in this region, such comparisons have been made problematical by the difficulty of ascertaining the appropriate theoretical scattering energy. We recommend here a protocol for resolving this problem for both elastic scattering and vibrational excitation.

PACS number(s): 34.80.Gs

I. INTRODUCTION

Molecular nitrogen has long been a fertile field for investigations of low-energy electron scattering. This system marks a transition between simple, moderately nonspherical few-electron systems and everything else and so has become a prototype for theoretical and experimental study of electron-molecule dynamics [1–6]. Beyond their fundamental relevance, low-energy e-N_2 cross sections are important to gas-discharge devices, laser-kinetic modeling, the physics of planetary atmospheres, and other applications [8–11]. Most prior theoretical work on e-N_2 focused on the broad, low-energy ($\sim$2.4 eV) $^2\Pi_g$ shape resonance, which induces dense, complicated oscillations in vibrationally elastic ($0\rightarrow 0$) and inelastic ($0\rightarrow v$) cross sections and dominates the energy range below about 4.0 eV [12–36]. In addition to early articulations of the nature of this resonance [14,15] and calculations of energies and widths (as a function of internuclear separation) using a wide range of theoretical methods [17,20], previous theoretical work elucidated the role of the resonance in vibrational excitation, primarily through the "boomerang model" [21–24], and led to increasingly sophisticated calculations of vibrational cross sections [24,35]. Of particular concern in these theoretical studies were the energies at which the differential cross sections (DCSs) and integral cross sections (ICSs) exhibit the prominent peaks that characterize this "intermediate lifetime resonance" [23–30]. Of the many previous experimental studies of low-energy elastic and vibrational e-N_2 scattering [37–58], several have focused on these important features [43,44,52,58].

By contrast, comparatively little attention has been given to determining *absolute* resonant or nonresonant cross sections at scattering energies below 10 eV. Neither experimental nor theoretical vibrational cross sections exist of an accuracy comparable to those for e-H_2, and extant results for this prototypical electron-molecule system are fragmentary [4,6]. The importance of determining these cross sections, whether by experiment or theory, follows from the key roles both resonant and nonresonant scattering play in low-energy e-N_2 collisions. The underlying physics of resonant scattering, e.g., the aspects of the electron-molecule interaction that control the collision and the region of configuration space that most influences distortion of the scattering function, differs from that of nonresonant scattering. Moreover, the nature of the nonresonant scattering is different below and above the resonance region, which extends roughly from 1.5 to 4.0 eV.

For both resonant and low-energy ($E < 1.0$ eV) nonresonant scattering, prior experimental and theoretical studies largely disagree [4,37–58]. Absolute DCSs for either $0\rightarrow 0$ or $0\rightarrow 1$ scattering have been measured by Ehrhardt and Willmann [38], Srivastava, Chutjian, and Trajmar [41], Shyn and Carignan [45], Tanaka, Yamamoto, and Okada [47], Brunger *et al.* [56], Brennan *et al.* [57], and Shi, Stephen, and Burrow [58]; comparisons of

*Permanent address: Department of Chemistry, The Sichuan Union University, Chengdu, Sichuan 610065, People's Republic of China.

the data from many of these experiments appear in the latter two papers. Integral cross sections can be determined from the results of some of the above DCS measurements by extrapolation to 0° and 180° followed by integration over the scattering angle. In addition, ICSs have been measured in attenuation experiments by Baldwin [40], Golden [42], Kennerly [46], Jost *et al.* [53], and Ferch, Raith, and Schweiker [55].

Of the innumerable theoretical investigations of low-energy e-N_2 scattering, absolute DCSs for $0\rightarrow 0$ and $0\rightarrow 1$ scattering are available from hybrid-theory calculations of Chandra and Temkin [34] and their completion by Weatherford and Temkin [35], Schwinger multichannel calculations of Huo *et al.* [29,30], close-coupling calculations by Morrison and Saha [36] and by Rumble, Truhlar, and Morrison [32,33], and R-matrix studies of Morgan [27] and of Gillan *et al.* [28]. In addition, explicitly resonant vibrational excitation in e-N_2 collisions has been explored in R-matrix calculations by Schneider, LeDourneuf, and Lan [25], optical-potential calculations by Berman *et al.* [26], via a model-based treatment by Wadehra and Drallos [31], and in numerous papers based on the aforementioned boomerang model [21–23].

The considerable differences one finds upon comparing results from the above experimental and theoretical studies often arise less from imprecision in one or another cross-section determination than from the difficulty in establishing meaningful points of comparison from two or more different studies. This problem is particularly acute in the resonance region, where the structure of the cross section is complex and highly sensitive to energy. This problem can be traced back to the initial observations by Schulz [37] and Ehrhardt and Willmann [38], which were subsequently confirmed by high-resolution measurements of Rohr [44], that the positions of the resonant peaks in e-N_2 elastic and vibrational cross sections depend sensitively on both the final vibrational state and the scattering angle. More recent discussions by Brennan *et al.* [57], Shi, Stephen, and Burrow [58], and Weatherford and Temkin [35] have foregrounded the key observation that within the resonance region, the vibrationally elastic DCSs at two energies separated by as little as 50 meV may differ radically in shape and absolute magnitude. (This problem, as we shall show, appears to be less acute for resonant inelastic scattering among low-lying vibrational states, where the shape of the cross section is largely independent of, and scales with, the energy.) We have made an important goal of the present collaborative study of low-energy e-N_2 scattering to articulate and test a protocol for meaningfully comparing theoretical and experimental DCSs in the resonance region. Since most electron-molecule systems manifest shape resonances below about 10 eV and many exhibit a distinctive (quasi)vibrational structure, the need for a meaningful way to make such comparisons extends well beyond the e-N_2 system.

In an effort to overcome these limitations of comparison, Shi, Stephen, and Burrow [58] have proposed an experimental protocol for DCS measurements according to which the incident energy in, say, an experimental and a theoretical study would be chosen *at each scattering angle* to correspond to the same structural feature in the resonance region. Although this technique would clearly remove any ambiguity in comparison between results from different experiments or from experiment and theory, we favor a different protocol as perhaps more practical. Our proposed protocol involves measurements at a fixed energy determined, for both experiment and theory, at corresponding structures in the experimental and theoretical cross sections, respectively. In particular, we here choose the resonance peaks in both the $0\rightarrow 0$ and $0\rightarrow 1$ cross sections at a predetermined angle. This protocol is discussed in more detail in Sec. V.

The present collaboration builds on previous work in e-N_2 scattering in the two groups involved. The earlier theoretical study by Morrison, Saha, and Gibson [61] centered on developing and testing a parameter-free model potential for polarization and bound-free correlation effects in the rigid-rotor approximation, where, of course, vibrational excitation cannot occur. The earlier experimental measurements of vibrational cross sections by Brennan *et al.* [57] were performed at only a few energies and used a different normalization technique than is implemented here. The present work represents a substantial increase in the accuracy and sophistication of both the experimental and theoretical techniques, as discussed in Secs. II–IV. In Secs. VI and VII we extensively compare elastic and inelastic ($0\rightarrow 1$) DCSs, total elastic cross sections, and grand total cross sections; the experimental ICSs in these comparisons were determined not by conventional extrapolation and integration methods but rather by a physically based fitting procedure we summarize in Sec. VII. Finally, we offer some concluding observations in Sec. VIII.

II. EXPERIMENTAL TECHNIQUES

A. Differential cross sections

The present experimental apparatus and the techniques used for obtaining absolute DCSs have been described in some detail previously [57,59]. However, as the current implementation of the relative flow normalization technique differs from that used in our previous e-N_2 studies [57], we shall provide a brief description that highlights these differences.

The apparatus is a conventional crossed electron–molecular-beam spectrometer that uses electrostatic hemispherical energy analyzers and electron optics to create and analyze incident and scattered electrons. Typical overall energy resolution for the present measurements is 40 meV at an incident electron beam current that varies between 0.5 and 2.0 nA, depending on incident energy. The incident energy scale was established by determining the position of the second resonance peak in the elastic e-N_2 DCSs at a scattering angle of 60°; as measured by Rohr [44], the position of this peak is 2.198 eV.

Physical constraints limit data collection to scattering angles between $-20°$ and 130°. We established the 0° position to within $\pm 1°$ by observing the symmetry of the scattered signal at positive and negative angles. The ap-

paratus, which is constructed from nonmagnetic materials, is surrounded by several layers of magnetic shielding and three orthogonal pairs of Helmholtz coils, which reduce the ambient magnetic field in the region of the spectrometer to less than 1 mG.

In our previous measurements of e-N_2 DCSs [57], we established an absolute scale by the relative flow technique [41,60], applying this normalization technique, which involves measuring relative elastic scattering intensities at several angles between the gas of interest and a reference gas, usually helium, to the measured angular distribution. The efficiency of the analyzer as a function of angle was checked against the shape of the e-He cross section [62]. In recent work on other systems (see, e.g., Ref. [63]) we have improved the efficiency and accuracy of our cross-section measurements by applying the relative flow technique *at each scattering angle.* This procedure, applied in the present e-N_2 measurements, removes within reasonable limits the dependence of the cross section on the size and shape of the interaction volume. Moreover, both gases are present in the scattering chamber at all times during the measurements; this procedure, which aids in maintaining operational stability and energy calibration, was first used and described by Shi, Stephen, and Burrow [58].

For the present measurements, the atomic beam was formed by a multicapillary array, which has been discussed previously. The experiments were conducted under the general guidelines established in a recent study of the shape of effusive molecular beams and the dependence of this shape on pressure and species [64]. This requires adjusting gas pressures at the entrance to the capillary array so that the mean free paths λ of the two gases are identical. To meet the secondary condition imposed by Buckman *et al.* [64], that λ be greater than twice the diameter of the capillary (40 μm), we kept the driving pressures for He and N_2 less than 1.0 and 0.7 Torr, respectively.

As the energy resolution is clearly not sufficient to resolve rotational structure, the experimental data were collected by scanning the analyzer energy loss across the entire energy-loss peak for elastic or inelastic ($0\rightarrow 1$) scattering and recording the analyzed electron signal in a multichannel analyzer (MCA). Thus *the measurements yield rotationally averaged elastic and vibrational excitation cross sections.* The MCA channel address was stepped in sequence with the energy-loss voltage and the mid-element of the analyzer optics zoom lens was swept over a predetermined range to maintain optimum transmission for both elastically and inelastically scattered electrons. As the absolute inelastic cross sections are determined by measuring intensity ratios to the elastic channel, it is important to consider the transmission of the analyzer for the elastically and the inelastically scattered electrons. In previous experiments, where the ratio of the outgoing energies was large, we investigated the transmission of the analyzer by measuring the yield of ejected and scattered electrons following near-threshold ionization of helium and used the predictions of the Wannier theory to estimate the analyzer transmission as a function of energy [65]. Because the greatest difference between the elastic and the inelastic scattered electron energies in the present measurements (for an incident energy of 1.98 eV) is about 15%, we have not applied this technique, which has an associated uncertainty of the order of 10%, but rather have relied on optimization of the electron zoom lenses to minimize transmission differences. Data accumulation was performed entirely under computer control.

The absolute uncertainty in the elastic DCSs is a combination of random statistical errors and known systematic errors due to the following factors: uncertainty in the relative flow calibration (5%); uncertainty in the e-He cross section, which is taken to be 2%; and drifts in electron-beam current and molecular-beam number density (1–2 %). The overall uncertainty, which is the addition in quadrature of random and systematic effects, is typically between 6% and 10%. The vibrationally inelastic cross sections have an additional uncertainty due to the transmission of the analyzer, which we estimate to be less than 10%.

B. Total cross sections

The second class of measurements reported in this paper is of the grand total cross section: the sum of cross sections for elastic scattering and all energetically accessible inelastic channels. These measurements were carried out using a linear time-of-flight (TOF) electron spectrometer, which has been described previously [63,66]. This apparatus has differentially pumped source, collision and detector regions, and a scattering cell with a length of 255 mm and entrance and exit apertures 1.0 mm in diameter. Electrons produced from a tungsten filament are accelerated, collimated, and formed into a pulsed beam by a series of electrostatic electron optical elements. The pulsed beam, with an energy of 200 eV, a repetition rate of (typically) 250 kHz, and a temporal width of 500 ps, is retarded in energy before it enters the scattering cell. By careful adjustment of the electron optics, electrons with a wide range of energies can be injected into the scattering cell. Indeed, at low energies it is possible to exploit most of the width of the thermal Maxwellian distribution from the hot filament so that cross sections can be measured simultaneously over an energy range of a few eV. The absolute energy of the electrons is obtained from their measured time-of-flight with an uncertainty that varies from 1 meV at 100 meV to about 50 meV at 2.5 eV. The electron count rates are such that at any one time there is at most only one detectable electron in the scattering cell.

Typical operating pressures, as measured with a calibrated spinning rotor viscosity gauge, were in the range from 5×10^{-4} to 2×10^{-3} mbar. Normal procedures were followed to ensure that multiple scattering was negligible. Cross sections were measured over a fine energy grid from 80 meV to about 4 eV. At higher energies, we made measurements at discrete 1-eV integrals to a maximum energy of 10 eV. The absolute uncertainty in these measurements of the grand total cross section, which is a combination of random statistical errors (typically less than 1%) and known systematic effects such as the uncertainty in the pressure determination (2%) and the scattering path length (1%), lies typically between

3% and 5%. The energy resolution varies from an estimated 10 meV or less at low energies to around 50 meV in the resonance region and above.

III. THEORY

In Sec. III A we describe the approximations inherent in our theoretical calculations, identify key quantities in determining the numerical precision of the theoretical DCSs presented in Sec. VI, and summarize our procedures for solving the e-N_2 scattering equations for the reactance (K) matrix we use to calculate the reported cross sections.

A. Collision dynamics

The essential dynamical approximations underlying the present theoretical calculations are first that the molecule does not undergo electronic excitation and second that rotational motion of the target can be treated adiabatically. Both are appropriate for e-N_2 elastic scattering and vibrational excitation at energies from a few tenths of an eV to several eV [1,3,94]. We incorporate the first approximation by projecting out of the electron-molecule Schrödinger equation the (Born-Oppenheimer) ground electronic state wave function and allowing for virtual electronic excitation (polarization effects) via a correlation-polarization potential to be described in Sec. III B. We incorporate the second by "freezing" the orientation of the internuclear axis in the solution of the scattering equations. This is the fixed-nuclear-orientation (FNO) approximation, the foundation of the adiabatic-nuclear rotation method for calculating approximate rotational excitation cross sections [67–89]. Since we are here interested in vibrational excitation cross sections, we (in effect) average the resulting FNO cross section over all molecular orientations. This produces a "total" FNO cross section for a vibrational transition $v_0 \rightarrow v$ that formally equals the sum of rovibrational cross sections for all energetically allowed transitions $v_0 j_0 \rightarrow v j$; in the FNO approximation this sum is independent of j_0.

In practice, we calculate the laboratory-frame DCS as an expansion in Legendre polynomials of the laboratory-frame (for which we use primed coordinates) scattering angle θ',

$$\left.\frac{d\sigma}{d\Omega}\right|_{v_0\rightarrow v} = \frac{1}{4k_0^2}\sum_{L=0}^{L_{\max}} B_L(v_0\rightarrow v) P_L(\cos\theta') \ , \tag{1}$$

where the maximum order $L_{\max}$ must be determined empirically and will depend on the particular transition and on the kinetic energy $k_0^2/2$ of the incident electron. The expansion coefficient $B_L(v_0\rightarrow v)$ contains the elements of the transition matrix [7]

$$\mathsf{T}^{\Lambda} = \frac{1}{2i}(\mathsf{S}^{\Lambda} - 1) \tag{2}$$

for the transition of interest

$$B_L(v_0\rightarrow v) = \sum_{\Lambda,\bar{\Lambda}} \sum_{l,\bar{l}} \sum_{l_0,\bar{l}_0} d_L(l l_0, \bar{l}\,\bar{l}_0; \Lambda\bar{\Lambda}) T^{\Lambda}_{vl,v_0 l_0} T^{\bar{\Lambda}*}_{v\bar{l},v_0\bar{l}_0} \ . \tag{3}$$

The additional coefficient $d_L(l l_0, \bar{l}\,\bar{l}_0; \Lambda\bar{\Lambda})$ contains details of the angular-momentum coupling

$$d_L(l l_0, \bar{l}\,\bar{l}_0; \Lambda\bar{\Lambda}) = i^{l_0 - l - \bar{l}_0 + \bar{l}} \frac{1}{2L+1} [(2l+1)(2\bar{l}+1)(2l_0+1)(2\bar{l}_0+1)]^{1/2} \times C(l\bar{l}L;0,0) C(l\bar{l}L;\Lambda,-\Lambda) C(l_0\bar{l}_0 L;0,0) C(l_0\bar{l}_0 L;-\bar{\Lambda},\bar{\Lambda}) \ . \tag{4}$$

The channel labels on the T matrix are $(v,l;\Lambda)$, where the quantum numbers correspond to the vibrational Hamiltonian (v), the orbital angular momentum of the projectile (l), and the projection of this angular momentum along the internuclear axis (Λ). The latter is a good quantum number in the FNO approximation [70], i.e., the FNO Hamiltonian commutes with the corresponding operator and the transition matrix is therefore diagonal in Λ. To exploit this fact we express the scattering equations in a body-fixed (BF) reference frame whose z axis is coincident with the (fixed) internuclear axis $\hat{R}$; unprimed coordinates refer to the body frame.

In contrast to the DCS (1), the computation of which often requires a large number of expansion coefficients $B_L(v_0\rightarrow v)$, the ICS and the momentum-transfer cross section are determined by only the $L=0$ and 1 coefficients as

$$\sigma_{v_0\rightarrow v} = \frac{\pi}{k_0^2} B_0(v_0\rightarrow v) \ , \tag{5}$$

$$\sigma^{(m)}_{v_0\rightarrow v} = \frac{\pi}{k_0^2}[B_0(v_0\rightarrow v) - \tfrac{1}{3} B_1(v_0\rightarrow v)] \ . \tag{6}$$

Although the BF FNO formulation treats the rotational motion of the nuclei adiabatically, it incorporates the vibrational dynamics exactly [7,34,35,71]. In the present implementation we obtain the BF FNO scattering equations by expanding the e-N_2 system wave function in the complete set of reduced N_2 vibrational wave functions $\{\varphi_v(R)\}$. To obtain a sufficiently accurate representation of target vibration for comparison to experiment, we have found it essential to use a basis of Morse wave functions. These are eigenfunctions of the one-dimensional Morse Hamiltonian with the potential [72]

$$V^{(M)}(x) \equiv D_e(1 - e^{-\alpha_M x})^2 \ , \tag{7}$$

which we have written in terms of the dimensionless variable $x = (R - R_{\rm eq})/R_{\rm eq}$. We find that the choice of parameters $D_e = 0.4480 E_h$, $\alpha_M = 2.5885 a_0^{-1}$, and $R_e = 2.02 a_0$ reproduces the energies of the lowest 15 vibrational states of N_2 to four decimal places [73]. In practice, we include in the vibrational eigenfunction expansion a sufficient number of terms N_v to converge reported cross sections to 1% or better.

To reduce the vibrationally coupled equations resulting from this expansion to a set of radial equations we further expand the wave function in a complete set of angular-momentum eigenstates for the scattering electron. In the BF reference frame, with $\hat{R}$ as the axis of spatial quantization, this is just the set of spherical harmonics $\{Y_l^{\Lambda}(\hat{r})\}$. We include in this second expansion N_l terms as required by our convergence criteria on the reported cross sections. The full expansion of the e-N_2 continuum function is

$$\Psi^{\Lambda}(\mathbf{r},R)=\frac{1}{r}\sum_{v=0}^{v_{\max}}\sum_{l}^{l_{\max}} u^{\Lambda}_{vl,v_0l_0}(r)\varphi_v(R)Y_l^{\Lambda}(\hat{r}) \ . \tag{8}$$

As summarized below, the number of both vibrational states N_v and partial waves N_l differs for resonant or nonresonant scattering and, in the latter case, on whether the energy is above or below the resonance region.

These expansions reduce the continuum e-N_2 Schrödinger equation to a set of coupled radial integro-differential equations the solution of which leads (via the radial wave-function matrix) to the transition (T) matrix that appears in the cross section coefficients (3). Considerable simplification in the structure of this matrix arises; since Λ is a good quantum number in the FNO approximation and the BF wave function is independent of the sign of Λ, the scattering equations separate into distinct sets identified by $|\Lambda|=0,1,\ldots$ and, for homonuclear targets, by parity, as *gerade* or *ungerade*. These simplifications lead to independent T matrices characterized by symmetry classes $\Sigma_g,\Sigma_u,\Pi_u,\Pi_g$, etc. Equation (3) shows that different symmetries in the DCS (1) "interfere" via products of T-matrix elements. By contrast, integrated BF FNO cross section separates according to symmetry class as

$$\sigma_{v_0\to v}=\sum_{\Lambda}\sigma^{\Lambda}_{v_0\to v} \ , \tag{9}$$

where the BF FNO cross-section partial in Λ is

$$\sigma^{\Lambda}_{v_0\to v}\equiv\frac{\pi}{k_0^2}\sum_{l=0}^{l_{\max}}\sum_{l_0=0}^{l_{\max}}|T^{\Lambda}_{vl,v_0l_0}|^2 \ . \tag{10}$$

Since for any value of $|\Lambda|>0$, the projection quantum number can assume values $\pm\Lambda$, there is implicit in Eq. (9) a multiplicative factor of 2 for each partial cross section except those of the Σ_g and Σ_u symmetries.

In practice, it is more convenient to solve the scattering equations for the (real, symmetric) reactance matrix K^{Λ}, which we can convert to a T matrix via

$$\mathsf{T}^{\Lambda}=\mathsf{K}^{\Lambda}(1-i\mathsf{K}^{\Lambda})^{-1} \ . \tag{11}$$

This K matrix arises from the asymptotic form of the BF FNO radial functions as [74]

$$u^{\Lambda}_{vl,v_0l_0}(r)\underset{r\to\infty}{\sim}\hat{j}_{l_0}(k_0r)\delta_{l,l_0}\delta_{v,v_0}+\left[\frac{k_0}{k_v}\right]^{1/2}\hat{n}_l(k_vr)K^{\Lambda}_{vl,v_0l_0} \ , \tag{12}$$

where $\hat{j}_{l_0}(k_0r)$ and $\hat{n}_l(k_vr)$ are the Ricatti-Bessel and Ricatti-Neumann functions for the entrance and the exit channels, respectively [75]. The radial functions satisfy the coupled differential equations [7]

$$\left[\frac{d^2}{dr^2}-\frac{l(l+1)}{r^2}-2V^{\Lambda}_{vl,vl}(r)+k_v^2\right]u^{\Lambda}_{vl,v_0l_0}(r)=2\sum_{v',l'\neq v,l}[V^{\Lambda}_{vl,v'l'}(r)u^{\Lambda}_{v'l',v_0l_0}(r)] \ , \tag{13}$$

where the coupling potential $\mathsf{V}^{\Lambda}(r)$ includes static, exchange, and correlation-polarization terms we shall describe below. The structure of this potential is

$$V^{\Lambda}_{vl,v'l'}(r)=\sum_{\lambda=0}^{\lambda_{\max}}g_{\lambda}(ll';\Lambda)w^{\lambda}_{v,v'}(r) \ , \tag{14}$$

where the angular coupling coefficient is

$$g_{\lambda}(ll';\Lambda)=\left[\frac{2l'+1}{2l+1}\right]^{1/2}C(l'\lambda l;\Lambda 0)C(l'\lambda l;00) \tag{15}$$

and the vibrational coupling potential, written in terms of Legendre projections $v_{\lambda}(r)$ of the interaction potential, is

$$w^{\lambda}_{v,v'}(r)\equiv\langle\varphi_v|v_{\lambda}|\varphi_{v'}\rangle=\int_0^{\infty}\varphi_v^*(R)v_{\lambda}(r,R)\varphi_{v'}(R)dR \ . \tag{16}$$

In practice we evaluate these integrals on the following grid of R values (in a_0): 1.60,1.70,1.80,1.85,1.90,1.95, 2.00,2.02,2.068,2.10,2.20,2.30,2.40,2.50. This grid, which is used throughout these BF FNO studies, exceeds the range of the (low-lying) vibrational wave functions of greatest importance to the particular excitations we are investigating. Although the Hartree-Fock N_2 electronic functions used in these calculations (discussed below) do not dissociate properly, the depth and narrowness of the N_2 electronic energy curve are such that this limitation is not significant for the process of primary interest here (see Fig. 3 of Ref. [84]).

The solution of Eq. (13) proceeds via the integral-equations algorithm [7,76], in which we first convert the integro-differential radial scattering equations to a set of coupled integral equations, then reduce this set to Volterra form. We solve the resulting equations by numerical propagation from the origin to the asymptotic region, as detailed elsewhere [77].

For e-N_2 and other typical electron-molecule systems, the dimensionality of the radial solution matrix $N_v\times N_l$ may become quite large if a large number of partial waves is required to accommodate the strongly nonspherical static potential in the near-target (small-r) region. Outside this region, however, the potential is comparatively weak, far fewer partial waves are required, and we can truncate the solution matrix [78]. For e-N_2 scattering below 10 eV, we truncate to $N_l=3$ partial waves at a truncation radius $r_{\text{trunc}}=6.0a_0$. This gambit significantly reduces the CPU demands of the propagation from r_{trunc} to $r_{\max}=85a_0$, except at low energies. The latter radial value is large enough that the K matrix does not change significantly beyond it. But below a few tenths of an eV (depending on the scattering process of interest), the

cross section is influenced by the potential at very long range; these weak but important effects can be incorporated into the K matrix rapidly, efficiently, and analytically using "Born r closure," a procedure we have elaborated in Ref. [7].

The question of how many partial waves we require for convergence arises in a different way when we use the close-coupling T matrix from Eq. (11) in the expansion coefficients (3) to calculate a particular DCS. The latter equation entails four summations over partial wave order (to upper limit $l_{\max}$) and two over the projection quantum number Λ (to upper limit $\Lambda_{\max}$) and these sums may run to quite large upper limits, particularly at small scattering angles. This situation does not, however, necessitate enormous close-coupling calculations. Rather, we can accurately augment low-order elements from the close-coupling T matrix with high-order elements calculated in the first Born approximation (FBA).

Elements of the K matrix corresponding to high partial-wave order l are strongly influenced by competition between two terms on the left-hand side of the coupled equations (13): the repulsive centrifugal barrier and the predominantly attractive diagonal potential matrix element $2V^{\Lambda}_{vl,vl}(r)$. Because of the barrier, high-l K-matrix elements are determined primarily by the long-range potential, which contains only static (Coulomb) and induced polarization terms. Specifically, this long-range coupling potential involves vibrational matrix elements of the spherical and nonspherical polarizabilities of the target $\alpha_0(R)$ and $\alpha_2(R)$ and of the permanent quadrupole moment $q(R)$; for electron scattering, it is given by Eq. (15) with

$$w^{\lambda}_{v,v'}(r) \underset{r\to\infty}{\sim} -\frac{\langle\varphi_v|\alpha_0(R)|\varphi_{v'}\rangle}{2r^4}\delta_{\lambda,0} - \left[\frac{\langle\varphi_v|q(R)|\varphi_{v'}\rangle}{r^3} + \frac{\langle\varphi_v|\alpha_2(R)|\varphi_{v'}\rangle}{2r^4}\right]\delta_{\lambda,2} . \tag{17}$$

This slowly varying long-range potential is weak enough that for l sufficiently large, the BF FNO K matrix elements may be approximated to high accuracy by their FBA counterparts [94]. For elastic scattering, these are

$$K^{\Lambda}_{v_0 l,v_0 l_0} = \frac{\pi k_0^2\langle\varphi_{v_0}|\alpha_0|\varphi_{v_0}\rangle}{(2l+3)(2l+1)(2l-1)}\delta_{l,l_0} + \frac{\pi k_0}{4}\left[\frac{2l_0+1}{2l+1}\right]^{1/2} C(l_0 2l;\Lambda 0)C(l_0 2l;00) \times\left[\frac{4k_0\langle\varphi_{v_0}|\alpha_2|\varphi_{v_0}\rangle}{(2n+3)(2n+1)(2n-1)\Gamma(-m+2)\Gamma(m+2)} + \frac{\langle\varphi_{v_0}|q|\varphi_{v_0}\rangle}{n(n+1)\Gamma(-m+\frac{3}{2})\Gamma(m+\frac{3}{2})}\right], \tag{18}$$

where $n\equiv(l+l_0)/2$ and $m\equiv(l-l_0)/2$. The form of the inelastic Born matrix elements is a little more complicated and so is most easily expressed in terms of the angular-momentum coupling coefficients of Eq. (15),

$$K^{\Lambda}_{vl,v_0 l_0} = -2\sqrt{k_v k_0}\sum_{\lambda} g_{\lambda}(ll_0;\Lambda)R_{\lambda}(vl,v_0 l_0) , \tag{19}$$

where the sum over λ includes only $\lambda=0$ (for the long-range spherical polarizability term) and $\lambda=2$ (nonspherical polarizability and permanent quadrupole terms). The inelastic FBA radial integral

$$R_{\lambda}(vl,v_0 l_0)\equiv\frac{1}{k_v k_0}\int_0^{\infty}\hat{j}_l(k_v r)w^{\lambda}_{v,v_0}(r)\hat{j}_{l_0}(k_0 r)dr \tag{20}$$

evaluates to

$$R_{\lambda}(vl,v_0 l_0)=\sum_{s_\lambda} B_{vv_0}(\lambda,s_\lambda)\frac{\pi k_v^l}{2^{s_\lambda}k_0^{\,l-s_\lambda+3}}\frac{\Gamma\left[\frac{l+l_0-s_\lambda+3}{2}\right]}{\Gamma\left[\frac{-l+l_0+s_\lambda}{2}\right]\Gamma\left[l+\frac{3}{2}\right]}F\left[\frac{l+l_0-s_\lambda+3}{2},\frac{l-l_0-s_\lambda+2}{2},l+\frac{3}{2},\frac{k_v^2}{k_0^2}\right] . \tag{21}$$

Here s_λ is the power of $1/r$ in the asymptotic (analytic) form of the potential [see Eq. (17)] and F is the hypergeometric function. For the present case, the only non-negligible long-range moment matrix elements in this expression are

$$B_{vv_0}(0,4)=-\tfrac{1}{2}\langle\varphi_v|\alpha_0|\varphi_{v_0}\rangle \quad(\lambda=0,\ s_\lambda=4) , \tag{22a}$$

$$B_{vv_0}(2,3)=-\langle\varphi_v|q|\varphi_{v_0}\rangle \quad(\lambda=2,\ s_\lambda=3) , \tag{22b}$$

$$B_{vv_0}(2,4)=-\tfrac{1}{2}\langle\varphi_v|\alpha_2|\varphi_{v_0}\rangle \quad(\lambda=2,\ s_\lambda=4) . \tag{22c}$$

All these FBA K-matrix elements are well defined except in the Σ_g symmetry, where the FBA radial integral for $\Lambda=l=l_0=0$ diverges. This poses no problem in practice

since we use close-coupling K-matrix elements for low-l channels in this symmetry.

To apply these results we identify (empirically) a "Born order" l_{Born} such that all elements with $l \geq l_{\text{Born}}$ are given by the FBA to sufficient accuracy to converge the desired cross section(s) to the desired precision. These Born elements augment the lower-order close-coupling elements in each of the Σ and Π K matrices in Eq. (3). We also identify a "Born symmetry" $\Lambda_{\text{Born}} > 0$ such that all K matrices with $|\Lambda| \geq \Lambda_{\text{Born}}$ are constructed entirely of FBA elements. In the present calculations, all Σ and Π K-matrix elements, *except those of the lowest three partial-wave orders,* are treated in the FBA, as are all the K matrices for $|\Lambda| \geq \Lambda_{\text{Born}} = 2$. This "Born l completion" procedure is essential to converge the DCS but not needed for the ICS.

B. Interaction potential

Low-energy vibrational excitation is acutely sensitive to all three constituents of the electron-molecule interaction potential [1,2]

$$V_{\text{int}}(\mathbf{r},R) = V_{\text{st}}(\mathbf{r},R) + V_{\text{ex}}(\mathbf{r},R) + V_{\text{CP}}(\mathbf{r},R) \ . \qquad (23)$$

These are first, the electrostatic term arising from Coulomb interactions between the projectile and the nuclei and electrons of the target, second, the exchange term arising from the antisymmetrization requirement on the e-N_2 wave function, and third, the correlation-polarization potential arising at short range from bound-free many-body effects and at long range from induced polarization effects. All three terms are nonspherical and, strictly speaking, the last two are nonlocal and depend on the scattering energy. In the present calculations we approximate these by local model potentials described below.

Operationally, we calculate the static, exchange, and correlation-polarization potentials from an R-dependent near-Hartree-Fock (HF) wave function for the $X\,^1\Sigma_g^+$ Born-Oppenheimer ground electronic state of N_2. This, in turn, we construct from the occupied molecular orbitals of the ground-state configuration $1\sigma_g^2 1\sigma_u^2 2\sigma_g^2 2\sigma_u^2 3\sigma_g^2 1\pi_u^4$, which we obtain by solving the HF self-consistent-field equations in a basis of R-dependent, contracted nucleus-centered Cartesian Gaussian functions [79]. Each of these basis functions is a $(9s5p1d/5s3p1d)$ contraction of a $(9s5p)$ nitrogen basis [80] augmented by an additional $3d$ function to facilitate bond formation [81].

To calculate the static potential $V_{\text{st}}(\mathbf{r},R)$, i.e., the average over the ground electronic state of the sum of all two-particle (bound-free) Coulomb potentials, we first generate from the occupied molecular orbitals the target charge density $\rho_0(\mathbf{r},R)$ on a mesh of internuclear separations [82]. From this quantity we evaluate the Legendre projections of the static potential $v_\lambda^{(\text{st})}(r,R)$ [83]. Because of a singularity in the electron-nuclear static potential at $r = R/2$, each Legendre projection contains a potentially troublesome cusp at this radius. But in the BF FNO scattering equations (13), these projections are embedded in coupling matrix elements (16). The integration over R in these integrals (16) smooths out this cusp and may reduce the number of partial waves required for convergence from that required in a rigid-rotor calculation, where the effect of the singularity is unmediated [84].

The long-range forms of the Legendre projections of the static potential define the theoretical permanent moments of the molecule. So from the large-r behavior of the $\lambda = 2$ projection we can extract the R-dependent quadrupole moment that appears in the vibrational matrix elements (17). To assess its accuracy by comparison to measured values we must average $q(R)$ over the ground vibrational state. Doing so yields $\langle \varphi_0 | q(R) | \varphi_0 \rangle = -0.961 e a_0^2$, which compares favorably with the experimental value $-(1.04 \pm 0.07) e a_0^2$ determined from measurements of induced birefringence [85]. Beyond the Hartree-Fock level, multiconfiguration self-consistent-field calculations of the quadrupole moment (at the equilibrium bond length) yield $-1.20 e a_0^2$ [86].

Rigorously including the nonlocal, energy-dependent exchange potential, although feasible for e-H_2 scattering [87], is problematic for significantly more aspherical systems with significantly more electrons. The present e-N_2 vibrational excitation study is based instead on an extension by Hara to scattering problems of the familiar Slater average exchange potential for bound states [88,89]. As implemented by Morrison and Collins [90,91], Hara's model is modified by treating the quantity $I(R)$ in the local momentum as a theoretical parameter. The resulting "tuned free-electron-gas exchange" (TFEGE) potential has been shown to be viable and accurate for vibrationally elastic scattering (in the rigid-rotor approximation) [90–93] and for vibrational excitation of H_2 [87,94]. Implementation of the TFEGE model for vibrational excitation requires determining $I(R)$ for a range of internuclear separations that encompasses the vibrational wave functions included in the target-state expansion. In both rigid-rotor and vibrational excitation studies, we base this parameter entirely on theoretical calculations; it does not entail adjustment to any experimental cross sections. To obtain an e-H_2 exchange potential, for example, Morrison, Feldt, and Austin [94] determined this parameter $I(R)$ from the Σ_u eigenphase sum in the static-exchange approximation at a single energy just above the first vibrational threshold.

One of the major findings of the present theoretical effort is that an accurate TFEGE potential for e-N_2 vibrational excitation cannot be generated in this simple way. For e-N_2 scattering we seek a potential flexible enough to describe both resonant and nonresonant collisions at energies from a few tenths of an eV to several eV. Resonant vibrational excitation is notoriously sensitive to exchange effects because near a resonance the scattering function is predominantly localized in the region of the target. For shape resonances of intermediate lifetimes like the one in e-N_2 scattering, the subtle interaction between the vibrational motion of the nuclei and the projectile, as conceptualized by the boomerang model of Birtwistle and Herzenberg [22], further exacerbates this sensitivity. Moreover, while low-energy vibrational excitation of H_2 is dominated by scattering in a sin-

gle electron-molecule symmetry, e-N_2 collisions involve several symmetries. Thus, while vibrationally inelastic resonant e-N_2 cross sections are entirely determined by the Π_g T matrix, elastic resonant ICSs entail comparable contributions from the Π_g and the Σ_g transition matrices, with lesser contributions to the DCSs from the Σ_u and the Π_u symmetries. All four of these symmetries make significant contributions to nonresonant elastic and inelastic cross sections, the importance of each T matrix depending on the scattering energy and excitation of interest.

Details of the tuning procedure we have developed to accommodate systems like e-N_2 will appear in a forthcoming paper [95]. Suffice it to say here that we use separate R-dependent TFEGE potentials in Σ and Π symmetries. First we determine values of the tuning parameter $I^{\Sigma}(R)$ for the (nonresonant) Σ_g and Σ_u symmetries to reproduce the exact-exchange Σ_g eigenphase sum at 0.1 eV. Second, we determine $I^{\Pi}(R)$ for the resonant Π_g symmetry at each internuclear separation to *reproduce the correct resonance energy* $E_r(R)$ at that R. The resulting exchange potential is also sufficiently accurate for the Π_u symmetry, which is the least important of the four lowest symmetries for the cross sections of interest. All these tuning calculations must be based on potentials that include the correlation-polarization terms, another important contrast to the situation for e-H_2 scattering [93]. Extensive tests showed that the resulting e-N_2 TFEGE potential accurately reproduced the complicated energy and R dependences of the resonant and nonresonant scattering matrices.

We conclude this description of the e-N_2 interaction potential with the correlation-polarization term $V_{CP}(\mathbf{r},R)$. In the asymptotic region, this potential reduces to the analytic form (17), which depends only on the vibrationally averaged induced moments of the target. At intermediate distances, outside the target charge cloud but not in the asymptotic region, the local kinetic energy of the projectile is low enough that the bound electrons respond as though it were a fixed charged particle. So in this region the projectile's motion can be accurately treated as adiabatic and the dependence of the polarization potential on the projectile velocity neglected. To implement this approximation we calculate the polarization potential outside the charge cloud as the difference between the mean energies of the polarized and the unpolarized systems. The former mean energy is just the expectation value of the e-N_2 Hamiltonian with respect to a target electronic function that has been polarized by the electric field of the (fixed) projectile; the latter is the same expectation value calculated with respect to an *unpolarized* (neutral) electronic function. We generate both these expectation values with the linear variational method, using our neutral $X\,^1\Sigma_g^+$ basis augmented with selected diffuse functions to allow sufficient flexibility for polarization [61,96–98].

The resulting adiabatic potential accurately represents polarization effects outside the charge cloud; one measure of this are the long-range induced moments we extract from its $\lambda=0$ and 2 projections. Using spherical and nonspherical polarizabilities $\alpha_0(R)$ and $\alpha_2(R)$ extracted from these moments at $r=10a_0$, we find, after averaging over the ground vibrational state, the values $\langle\varphi_0|\alpha_0|\varphi_0\rangle=10.980a_0^3$ and $\langle\varphi_0|\alpha_2|\varphi_0\rangle=3.096a_0^3$. The first value compares favorably with the (room-temperature) experimental spherical polarizability $(11.744\pm0.004)a_0^3$ measured by Newell and Baird [99] and by Orcutt and Cole [100]. We can further assess this potential by comparing our nonspherical polarizabilities to estimates based on the relative polarizability anisotropy measured by Bridge and Buckingham [85]. For this estimate Miller and Bederson [101] report $(3.08\pm0.002)a_0^3$, a value in comparably good agreement with ours. Near the present HF level of representation of the ground electronic state of N_2 lie the multireference (singles and doubles) configuration-interaction results $11.52a_0^3$ and $3.16a_0^3$ of Langhoff, Bauschlicher, and Chong for the spherical and nonspherical polarizabilities [102]; these values vivify the observation that the nitrogen molecule is a "good [self-consistent field] molecule, in the sense that electron correlation is not very important for the calculation of the dipole polarizabilities" [103].

The most problematic region for the correlation-polarization potential is inside the target charge cloud. Here two effects come into play. First, the velocity dependence of $V_{CP}(\mathbf{r},R)$ may be important. Second, and more serious for low-energy e-N_2 scattering, in this region many-body effects are important. Inside the charge cloud the scattering electron is formally indistinguishable from the bound electrons. Hence the independent-particle model on which the adiabatic potential rests ceases to be viable; the resulting many-body effects yield a short-range nonlocal bound-free correlation potential for the small-r behavior of $V_{CP}(\mathbf{r},R)$.

Rigorously and accurately including these effects in low-energy electron-molecule calculations is extremely difficult even in the rigid-rotor approximation; recent efforts based on Green's functions and optical-potential theories are summarized in the introduction to Ref. [104]. We have chosen a less rigorous approach based on a parameter-free model potential that approximates short-range many-body effects via an *ad hoc* stratagem first proposed by Temkin [105] for electron-atom scattering. In this "nonpenetrating approximation," the polarization potential $V_{CP}(\mathbf{r},R)$ is corrected (i.e., weakened) in the short-range region by "turning off" the two-particle bound-free Coulomb interactions (in matrix elements of the variational calculation) whenever the coordinate of the projectile is less than that of one of the bound electrons. This yields a multipole expansion of which we retain only the dipole term. Hence we have dubbed the result the "better-than-adiabatic-dipole" potential [97,98,36]. Elsewhere we have provided extensive discussions of the generation of this R-dependent potential [98,61] along with details of its implementation for vibrational excitation [36] and a diagnosis of its strengths and weaknesses [104].

IV. CONVERGENCE MATTERS

Differential cross sections are notoriously more sensitive than integrated cross sections to physical and numer-

ical approximations. Because of the prototypical nature of low-energy e-N_2 scattering, this system can serve as a laboratory for developing criteria for accurate calculations of DSCs for other systems. Here we shall focus on the number of vibrational states and partial waves in the eigenfunction expansion of the e-N_2 wave function near the target and the number of partial waves and electron-molecule symmetries in the expression for the DCS in terms of BF FNO T-matrix elements.

The BF FNO close-coupling method sketched in the preceding section is predicated on an expansion of the electron-molecule wave function (for a particular symmetry class) of the form given in Eq. (8). In this section we are concerned with the number of vibrational states (N_v) and partial waves (N_l) one must include in these expansions *in the near-target region,* i.e., for $r < r_{\text{trunc}}$. (Outside this region we can truncate both expansions severely with no loss of accuracy.)

First, the number N_l of partial waves $Y_l^{\Lambda}(\hat{r})$ included in the expansion of the system wave function in the near-target region $r < r_{\text{trunc}}$ must allow fully for coupling by the nonspherical Legendre coefficients $v_\lambda(r,R)$ in the coupling potential (14). Second, the sums over partial-wave orders and projection quantum numbers in the expansion coefficient (3) must include enough terms to account for the often subtle interference effects exhibited in these DCSs. Finally, we must include a sufficient number N_v of vibrational states in the expansion of the system wave function.

A. Vibrational states

The number of vibrational states one must include in Eq. (8) depends rather loosely on the energy, especially on whether the scattering is resonant or nonresonant. For scattering below the resonance region, we require six states to converge the reported elastic and inelastic DCSs to 1% at energies from 0.02 to 0.32 eV and nine states at energies to 1.36 eV; above the resonance, from 5.0 to 10.0 eV, nine states again suffice.

Convergence in the resonance region is more interesting, the requisite number of states exhibiting considerable sensitivity to the energy. The $0 \rightarrow 0$ DCS at 2.45 eV (the theoretical energy of the third peak in the elastic DCS at 60°), shown in Fig. 1(a) is typical of elastic scattering in this energy range. Convergence requires 14 vibrational states, higher-lying states ($v > 8$) contributing primarily at $\theta < 30°$ and $\theta > 150°$. Similarly, the inelastic $0 \rightarrow 1$ cross section at this energy, shown in Fig. 1(b), is well converged only by $N_v = 14$. Such behavior is not, however, typical of inelastic cross sections. At 2.60 eV (the energy of the third peak in the $0 \rightarrow 1$ cross section), the inelastic $0 \rightarrow 1$ DCS in Fig. 1(c) exhibits nonmonotonic convergence, with $N_v = 6$ providing a surprisingly good expansion.

The essential point of these comparisons (apart from the warning implicit in nonmonotonic convergence) is that more vibrational states are required for resonant than for nonresonant scattering. This finding is expected from the nature of the resonance. As reviewed by Bardsley and Mandl [21], by Schulz [39,10], and by Lane [1], the e-N_2 shape resonance around 2.4 eV exemplifies a special case that is intermediate between the "compound molecule limit" (resonances of small widths that can be understood as temporary negative-ion complexes) and the "impulse limit" (very wide structures). Because polarization of the N_2 charge cloud by the projectile is significant

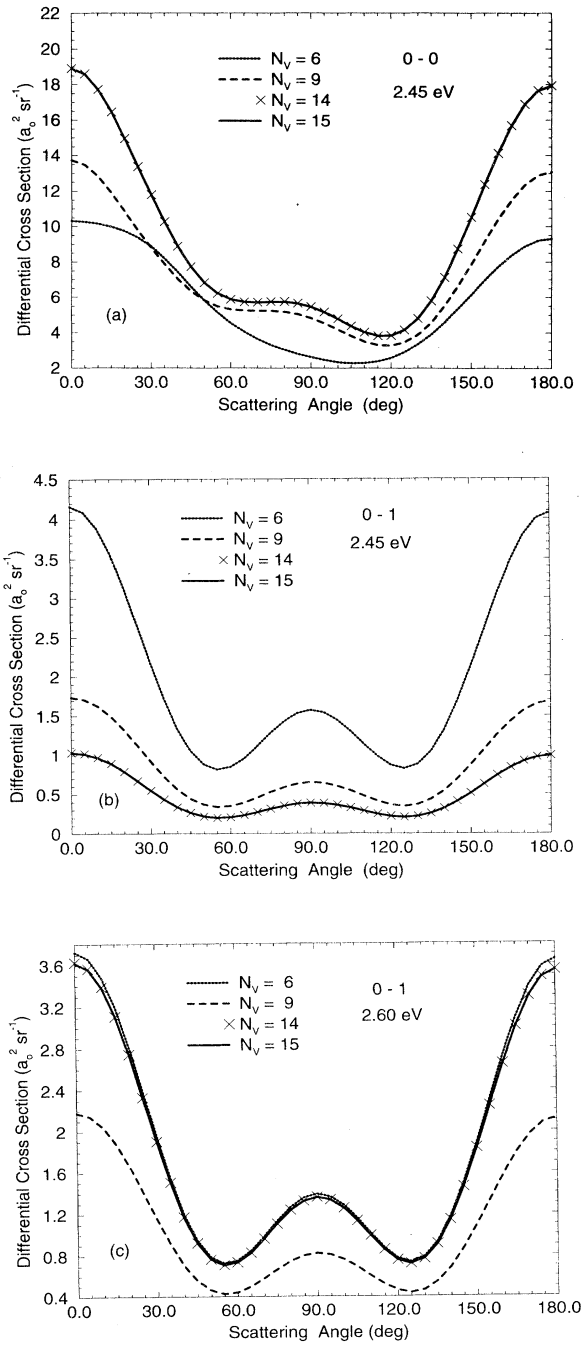

FIG. 1. Convergence in the number of vibrational states N_v of (a) the elastic e-N_2 DCS at 2.45 eV and the inelastic DCS at (b) 2.45 eV and (c) 2.60 eV. These results are converged in partial waves in the near-target region [see Eq. (8)] and in asymptotic partial waves and symmetries in the Legendre coefficients (3) of the DCS.

at such energies, the vibrational eigenfunctions of the Born-Oppenheimer Hamiltonian of the undistorted neutral, as used in Eq. (8), are not the most physically appropriate basis for the e-N_2 system in the resonance region. Although this basis is mathematically valid, it forces vibrational relaxation during the lifetime of the resonance into the coupling matrix elements $w^{\lambda}_{v,v'}(r)$ of Eq. (16), incorporating this effect through nonadiabatic coupling of the electronic and nuclear motion. Hence such an expansion may increase the number of basis functions required for convergence, as demonstrated in Fig. 1. Yet, as the boomerang model analysis of Birtwistle and Herzenberg clarifies, neither is an expansion in terms of vibrational states of the transient N_2^- complex physically appropriate. In fact, as articulated by Schneider [106], the most suitable representation is a "compound-state model" formulated around the "resonant" electronic state of the electron-molecule complex (e.g., with the R-matrix method) [26]. Extensive, sophisticated calculations of this resonance using such methods have been performed by Schneider, Le Dourneuf, and Lan [25], Hazi, Rescigno, and Kurilla [24], and Gillan *et al.* [28].

As a final caveat concerning representation of the vibrational dynamics in the resonance region, we emphasize that care must be exercised in determining the vibrational wave functions in the vibrational coupling potentials (16). In the present study, neither simple harmonic-oscillator functions nor numerical wave functions generated by solving the nuclear Schrödinger equation for a Hartree-Fock ground-state potential proved sufficiently accurate for resonant e-N_2 scattering; instead we use eigenfunctions of the Morse potential [72] with parameters based on the experimentally measured energy levels of the 15 lowest vibrational states [73].

B. Partial waves in the near-target region

The other critical expansion in the near-target region is the sum in Eq. (8) over BF spherical harmonics. The number of these partial waves required to converge a given DCS depends more critically than the number of vibrational states on the energy, the scattering angle, the excitation, and whether the scattering is resonant or nonresonant. Below the resonance, the magnitude of the elastic DCS is controlled largely by the Σ_g T matrix and its shape by Σ_u and Π_u. As illustrated at 0.55 eV in Fig. 2(a), the shape is given correctly by a seven-term partial-wave expansion while the magnitude requires $N_l = 11$

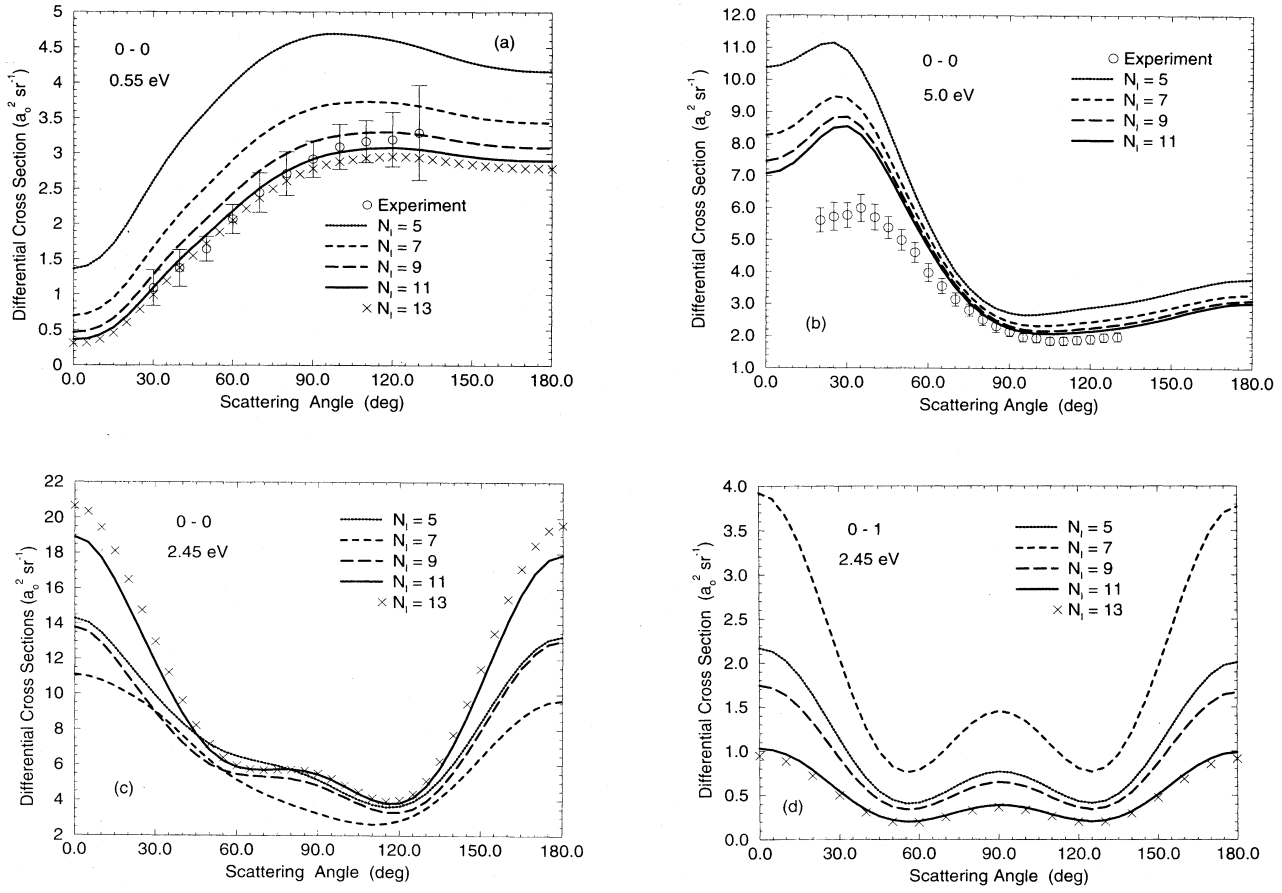

FIG. 2. Convergence in the number of partial waves N_l in the near-target region of the elastic e-N_2 DCS at (a) 0.55 eV, (b) 5.0 eV, and (c) 2.45 eV and of (d) the $0 \rightarrow 1$ DCS at 2.45 eV. These results are converged in vibrational states in Eq. (8) and in asymptotic partial waves and symmetries in the Legendre coefficients of the DCS, Eq. (3). The experimental data (open circles) in (a) and (b) are from the present crossed-beam measurements.

(i.e., $l_{max}=20$ in the Σ_g symmetry).

Above the resonance, forward scattering dominates the vibrationally elastic cross section. As illustrated by the 5.0-eV DCS in Fig. 2(b), including partial waves with $l \geq 5$ in the near-target expansion Eq. (8) is vital to converging the DCS for scattering angles below about 45°. [As discussed below, above-resonant small-angle scattering is also sensitive to the number of partial waves and symmetries included in the DCS sums in Eq. (3).] Convergence of the above-resonance $0 \rightarrow 1$ inelastic DCS (not shown) is quite smooth, with typically $N_l=9$ partial waves required at large angles. At still higher energies, these high-order partial waves are less important; by 10 eV (not shown), a seven-partial-wave expansion gives the shape and magnitude of the $0 \rightarrow 0$ DCS to 1% at all angles.

Convergence of the resonant inelastic DCS is marked by the importance of the Π_g symmetry. But for the resonant *elastic* DCS, illustrated at 2.45 eV in Fig. 2(c), we find the characteristic shape [see Eq. (1)] of a Π_g resonance modulated by contributions from other symmetries. The characteristic angular variation of a pure-resonant DCS, which is unmodulated for inelastic scattering, arises from the overwhelming dominance of the $l=l_0=2$ element of the Π_g T matrix in Eq. (3). The Clebsch-Gordan coefficients in Eq. (4) result in contributions to the DCS from Legendre polynomials $P_L(\cos\theta')$ for $L=0$, 2, and 4; the resulting DCS is large at forward and backward angles, has a minimum near 60° and 120°, and a small peak at 90°. The detailed shape, of course, depends on the particular admixture of Legendre polynomials that results from the T matrices for the energy and scattering process of interest. The skewed shape of the elastic DCS, which results from symmetries other than Π_g, is roughly approximated by few-partial-wave expansion and converged by $N_l=13$, with convergence slowest at forward and backward angles. No such modulation affects the $0 \rightarrow 1$ DCS, shown at 2.45 eV in Fig. 2(d), because Π_g dominates all inelastic e-N_2 DCSs. Convergence is attained by $N_l=11$.

C. "Asymptotic" symmetries and partial waves in the DCS

Thus far we have considered only the expansion (8) in partial waves of the near-target e-N_2 wave function; the number N_l of terms controls convergence of the (truncated) close-coupling T-matrix elements we extract from the asymptotic form of the radial functions $u^{\Lambda}_{vl,v_0l_0}(r)$. An entirely separate issue is the number of partial waves required to converge the Legendre coefficients $B_L(v_0 \rightarrow v)$ in the DCS (3). Each of these coefficients contains sums over the projectile orbital angular momentum quantum numbers in the entrance and the exit channels and over the corresponding projection quantum numbers with respect to $\hat{R}$, the BF z axis. Interference effects crucial to the DCS arise from terms containing T-matrix elements from different symmetry classes (e.g., Σ_g and Π_g) or different partial waves within a symmetry class. These high-order and high-symmetry terms correspond to "asymptotic partial waves"; they are not involved in converging the close-coupling T matrix and so, as discussed in Sec. III, are accurately (and very efficiently) given by their first Born approximates from Eq. (18).

To illustrate, we shall examine the convergence in Λ of typical elastic cross sections at energies below, in, and above the resonance region as well as convergence of a typical above-resonance inelastic DCS. [The maximum partial-wave order l_{max} and the Born order l_{Born} are much less sensitive to energy and excitation—and so are less interesting—than L_{max}. For the Σ and Π contributions to the DCS coefficients we use close-coupling T-matrix elements for the lowest three partial waves and augment these with FBA matrix elements for nine additional values of l. In all higher-order symmetries ($|\Lambda|>1$), which we include entirely via the FBA, we use 12 partial waves.] To generate the unconverged DCS in these figures we systematically included in the sums in Eq. (3) T matrices of successively higher-order symmetry class: the Σ curve in Fig. 3(a), for example, includes only $\Lambda=0$ matrix elements, with the sum over l completed to convergence.

We begin in Fig. 3(a) with the $0 \rightarrow 0$ DCS at 0.55 eV, whose convergence behavior typifies elastic scattering from 0.1 to 1.5 eV. Although the Σ_g T matrix is primarily responsible for the magnitude of the cross section at this energy, the Π symmetries, with $|\Lambda|=1$, determine the shape. High-order symmetries up to the convergence limit $|\Lambda|=7$ induce subtle but important alterations in the shape, especially at small and large angles.

Such high-order symmetries are largely irrelevant for resonant scattering. As illustrated by the 2.20-eV elastic cross section in Fig. 3(b), the shape of the DCS is essentially determined by the Π_g symmetry. The shape and the magnitude at all angles are given almost perfectly by the Π_g and the Σ_g T matrices, other contributions introducing negligible adjustments at small angles. This point may be clarified by noting that the 2.20-eV elastic Π_g integrated partial cross section $\sigma^{\Pi_g}_{0 \rightarrow 0}$ [see Eq. (9)] is in error by about 40%, while the sum of this and the Σ_g cross sections gives an ICS accurate to a few percent.

Above the resonance region, Π_g ceases to be the controlling symmetry. The characteristic 4.0-eV elastic cross section in Fig. 3(c) illustrates the importance of the Σ_g and the Σ_u symmetries to the shape and the magnitude of above-resonance elastic DCSs. Contributions for $2 \leq |\Lambda| \leq 7$ are essential to correctly reproducing the small-angle behavior of the elastic DCSs from 4.0 to 10.0 eV, where this cross section is characterized by a pronounced downturn with decreasing scattering angle $\theta < 60°$. These high-order symmetries do not, however, contribute to the corresponding ICSs, which are converged by $\Lambda_{max}=2$.

We now turn to the $0 \rightarrow 1$ DCSs. Below-resonance inelastic cross sections are extremely small and resonant inelastic DCSs exhibit no interesting convergence behavior, their shape and magnitude being entirely controlled by the Π_g symmetry. Above the resonance, however, quite different behavior obtains. At these energies low-order partial waves, which in our implementation pertain to close-coupling elements of the T matrix, are more penetrating than below the resonance and hence are sub-

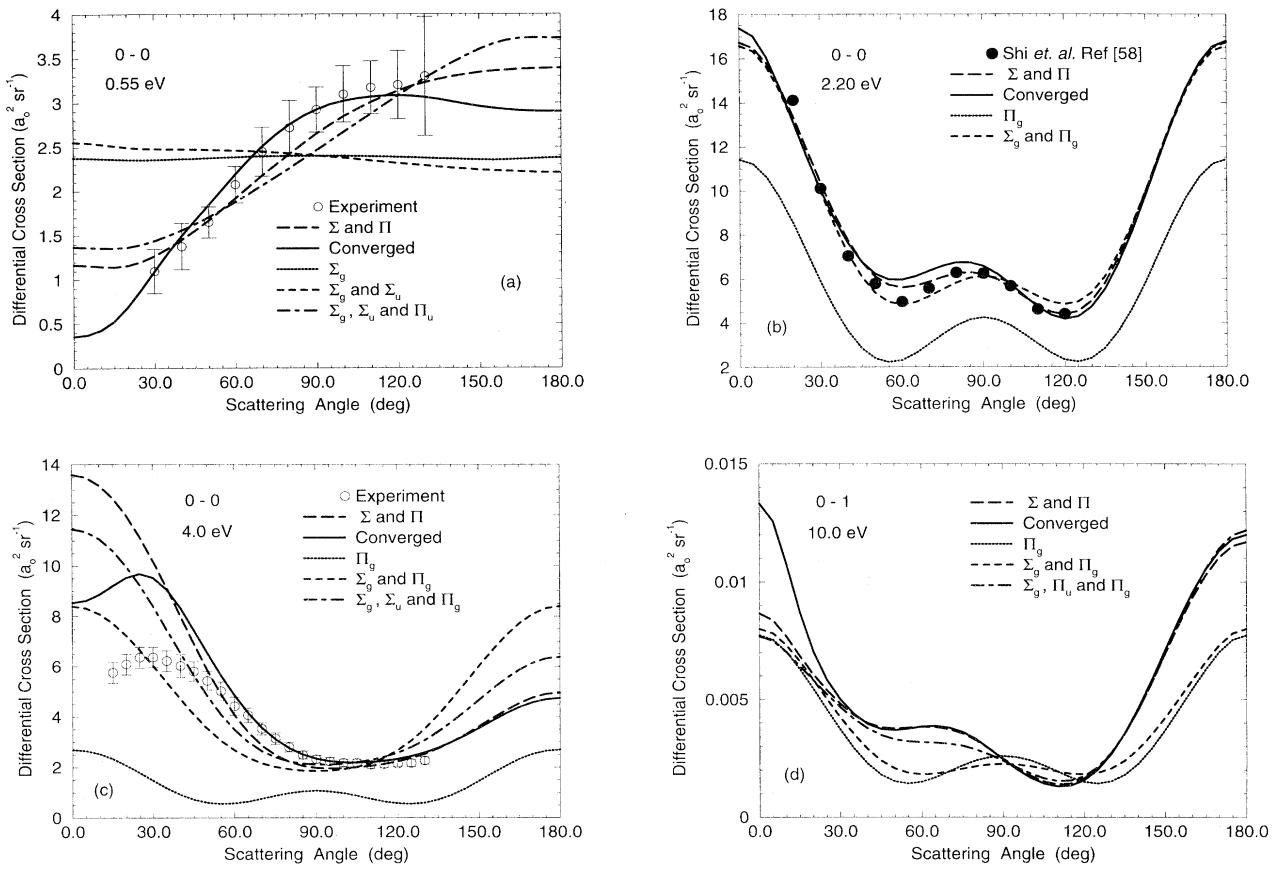

FIG. 3. Convergence in the number of electron-molecule symmetry classes included in the Legendre coefficients of the DCS for the elastic e-N_2 DCSs at (a) 0.55 eV, (b) 2.2 eV, and (c) 4.0 eV and of (d) the $0\rightarrow1$ DCSs at 10.00 eV. These results are converged in vibrational states and partial waves in the near-target region [see Eq. (8)]. The results designated "converged" (solid line) contain contributions from the first 16 symmetry classes. The experimental data (open circles) are from the present crossed-beam measurements.

ject to greater distortion. As the $0\rightarrow1$ cross section at 10.0 eV in Fig. 3(d) illustrates, these low-order partial waves essentially determine the DCSs except at small angles. Thus the DCS for $\theta>90°$ is entirely determined by the Σ_g, the Π_u, and the Π_g symmetries, while these symmetries and the Σ_u control intermediate-angle scattering $45°<\theta<90°$. Only for $\theta<45°$ do we require high-order symmetries ($\Lambda_{max}=8$) to converge the inelastic DCSs.

Although the specific partial-wave and vibrational-state requirements for accurate DCS calculation will, of course, vary from system to system, the general principles illustrated here should pertain to low-energy resonant and nonresonant elastic and inelastic scattering from nonpolar targets.

V. PROTOCOL FOR THE COMPARISON OF RESONANT CROSS SECTIONS

Much of the disagreement evident in previous published comparisons of experimental and theoretical electron-molecule cross sections at energies near an intermediate-duration shape resonance, like that in the e-N_2 system, may arise from the inappropriateness of the comparisons themselves. As several prior investigators have discussed [44,56–58], the acute dependence of the DCS on energy throughout the resonance region makes it imperative that comparisons be made at identical structural features (e.g., peaks and valleys) rather than at some value of the incident energy defined in measurements or calculations.

In the present work, where meaningful comparison between experiment and theory is essential, we have established a protocol whereby both *experimental and theoretical DCSs are determined at energies corresponding to structures in the resonance profile in either the $0\rightarrow0$ or the $0\rightarrow1$ channel.* As Table I demonstrates, the "absolute" energies at which many of these structures occur in experimental and theoretical cross sections do not agree. Since their energies vary with scattering angle, we have chosen a scattering angle of 60° as the point of comparison for experiment and theory. Note that this protocol does not limit such comparisons to structures in the cross section of interest; for example, in Sec. V B we compare elastic DCS measured and calculated at energies corresponding to a particular structure in the $0\rightarrow1$ inelastic cross section.

Thus, in addition to comparisons at energies below and above the resonance, we present in Sec. VI elastic and in-

TABLE I. Energy (in eV) of the resonance peaks in the 0→0 and 0→1 differential cross sections at a scattering angle of 60°. Also shown in parentheses are the valleys in the theoretical and the experimental DCS at 60°.

	Experiment		Theory	
Peak no.	Present	Rohr (Ref. [44])	DCS at 60°	ICS
		(a) Elastic channel		
1	1.92 (2.04)	1.924	1.90 (2.20)	1.95
2	2.198[a] (2.33)	2.198	2.20 (2.35)	2.20
3	2.46 (2.59)	2.451	2.46 (2.60)	2.484
4	2.71 (2.85)	2.700	2.70 (2.95)	2.80
5	2.96 (3.08)	2.934	3.10 (3.30)	3.10
6	3.20		3.50 (3.70)	3.40
		(b) Inelastic (0→1) channel		
1	1.98 (2.14)		1.95 (2.10)	1.95
2	2.30 (2.48)		2.30 (2.46)	2.30
3	2.61 (2.76)		2.60 (2.80)	2.60
4	2.89 (3.01)		3.00 (3.20)	3.00
5	3.13 (3.27)		3.35 (3.60)	2.25
6	3.37		3.75	3.75

[a]Energy for normalization to Rohr [44].

elastic (0→1) DCSs as measured and calculated at the positions of the first and the third resonance peaks in both channels at a scattering angle of 60°. Figure 4 shows the experimental and the theoretical energy dependences of these cross sections at this angle. The experimental data include both the "excitation functions," where the yield of scattered electrons for a particular process is measured as a function of incident energy, and values obtained from the DCS measurements (to be discussed below) at several energies. We emphasize that our choice of these particular peaks, although convenient, is not essential; rather the essential point is that comparisons be made at the same relative positions within the resonance envelope.

To be sure, other comparison protocols are possible. In fact, Shi, Stephen, and Burrow [58] have proposed an "energy optimized" protocol in which the scattering energy is changed as a function of scattering angle to ensure that measurements are made at the same structural position within the resonance at all angles. We consider our alternative protocol a reasonable compromise that is perhaps more pragmatic for the experimentalist and theorist.

VI. RESULTS: DIFFERENTIAL CROSS SECTIONS

A. Resonant inelastic (0→1) scattering

We have measured and calculated DCSs for resonant excitation of the first vibrational mode of N_2 at three energies that correspond to the first and the third peaks in the 0→1 excitation function and to the third peak in the 0→0 excitation function. As Table I shows, the latter comparison, which is determined by a structure in the elastic cross section, corresponds to the second *valley* in the theoretical 0→1 DCS at 60°. Our results are given in Tables II and III and compared in Fig. 5.

The inelastic 0→1 DCSs measured and calculated at the first peak in this cross section appear in Fig. 5(a); the experimental and theoretical energies for this comparison, from Table I, are 1.98 and 1.95 eV, respectively. The characteristic shape arising from the dominance of

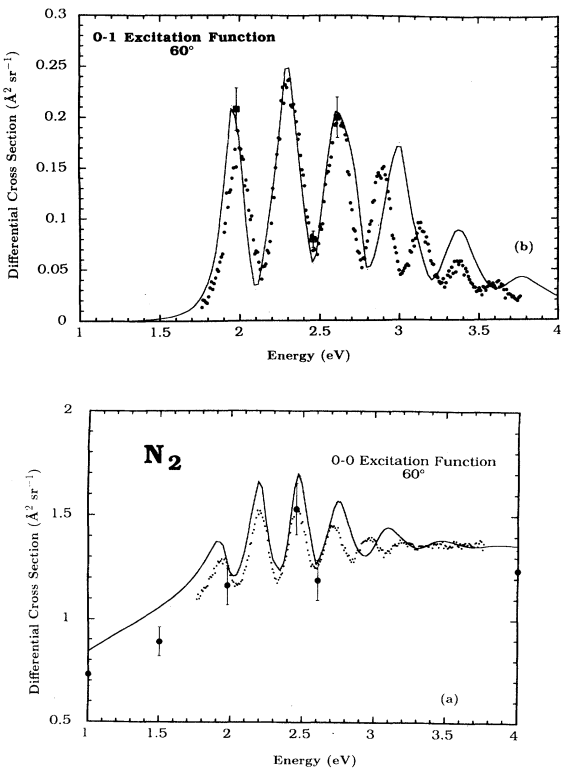

FIG. 4. Energy dependence of the (a) elastic and (b) inelastic (0→1) DCSs from theoretical (solid line) calculations compared to measured excitation functions (dots) and DCS data (solid circles).

TABLE II. Experimental resonant elastic (0→0) and inelastic (0→1) differential cross sections for e-N_2 scattering (10^{-16} cm^2 sr^{-1}) at incident energies chosen with reference to structures in the *measured excitation function* at 60°.

Angle	$v_0=0\rightarrow v=1$			$v_0=0\rightarrow v=0$			
(deg)	1.98 eV	2.46 eV	2.605 eV	1.92 eV	1.98 eV	2.46 eV	2.605 eV
15.0		0.313	0.849			4.960	2.829
20.0	0.749	0.269	0.716	2.046	2.304	4.522	2.637
25.0	0.621	0.241	0.623	1.732	1.978	4.114	2.508
30.0	0.523	0.187	0.514	1.479	1.771	3.604	2.311
35.0	0.420	0.156	0.415	1.299	1.511	3.194	2.120
40.0	0.333	0.128	0.328	1.168	1.348	2.740	1.892
45.0	0.267	0.097	0.267	1.111	1.252	2.334	1.691
50.0	0.231	0.080	0.223	1.093	1.207	1.975	1.520
55.0	0.208	0.072	0.199	1.139	1.171	1.735	1.336
60.0	0.208	0.080	0.200	1.220	1.169	1.530	1.189
65.0	0.230	0.086	0.226	1.345	1.217	1.403	1.082
70.0	0.261	0.101	0.255	1.479	1.269	1.307	0.978
75.0	0.307	0.109	0.299	1.580	1.385	1.301	0.941
80.0	0.357	0.126	0.331	1.687	1.430	1.332	0.883
85.0	0.379	0.132	0.360	1.775	1.450	1.286	0.841
90.0	0.396	0.142	0.368	1.776	1.450	1.303	0.800
95.0	0.398	0.141	0.365	1.722	1.419	1.275	0.758
100.0	0.374	0.135	0.361	1.650	1.348	1.218	0.742
105.0	0.352	0.123	0.323	1.536	1.274	1.155	0.710
110.0	0.315	0.111	0.288	1.437	1.178	1.088	0.696
115.0	0.272	0.098	0.256	1.301	1.092	1.056	0.714
120.0	0.246	0.088	0.230	1.184	1.021	1.095	0.741
125.0	0.214	0.079	0.211	1.101	1.001	1.150	0.815
130.0	0.199	0.075	0.206	1.022	0.994	1.335	0.912

the Π_g resonant inelastic e-N_2 T matrix is immediately obvious and agreement between experiment and theory is exceptionally good. At angles greater than about 100°, the experimental cross section appears to be shifted slightly towards higher angles than the theory, though both exhibit the characteristic angular dependence.

For our second comparison we consider an energy defined by the third peak in the elastic channel; this structure occurs at 2.46 eV in the measured excitation function, about 30 meV below the position of the second valley in the experimental 0→1 DCS at 60°. Accordingly, we compare to the theoretical DCS calculated at an energy 30 meV below the position of this valley in the theoretical 0→1 DCS at this angle, i.e., at 2.43 eV. Agreement between the two DCSs, which are shown in Fig. 5(b), is exceptionally good. This comparison illustrates the extension of the protocol in Sec. V to energies that are "off peak" for a particular excitation.

We make our final comparison of inelastic DCS at an energy corresponding to the third peak in the 0→1 excitation function; this peak occurs at 2.61 eV in the experimental and 2.60 eV in the theoretical results at 60° (see Table I). Here too agreement between the two cross sections is excellent at all angles. We have demonstrated convergence of these results in vibrational states and partial waves in Figs. 1(b) and 2(a), respectively.

To conclude, we note that the DCSs at these three energies exhibit differences in magnitude but not in shape. This reflects the relative position of the comparison energies within the resonance profile and the overwhelming dominance of resonant—as opposed to direct—scattering in vibrational excitation of N_2.

B. Resonant elastic scattering

In the resonance region we have measured and calculated elastic DCSs at four energies selected according to the protocol established in Sec. V. These cross sections, at experimental (theoretical) energies of 1.92 (1.90), 1.98 (1.95), 2.46 (2.46), and 2.61 (2.60) eV, which correspond to the first and the third peaks in the elastic and inelastic DCS at 60°, respectively, are listed in Tables II and III and are compared with prior experimental and theoretical results in Fig. 6. Agreement between the present experimental and theoretical DCSs is least satisfactory at the first of these energies, which corresponds to the first peak in the 0→0 DCS at 60°. As Fig. 6(a) shows, this disagreement is largest at angles less than about 30°. Nevertheless, the importance of the Π_g symmetry is clear in both results, but not in the DCS of Shyn and Carignan [45], which were also (apparently) measured at the first resonance peak in this channel. This difference may arise from somewhat lower-energy resolution in their measurements than in ours.

The elastic DCS at the energy of the first peak *in the 0→1 inelastic cross section* is shown in Fig. 6(b). This structure occurs at 1.98 eV in the measured excitation function and 1.95 eV in the calculated DCS; the corresponding inelastic cross sections were shown in Fig. 5(a). (Note that these energies are off the peak of the DCS in

the $0 \rightarrow 0$ channel.) Strikingly, the slight increase in energy (60 meV) from that of Fig. 6(a) results in substantial changes in the shape and magnitude of the elastic DCS. Agreement between experimental and theoretical results is also slightly better at this energy; both manifest a marked increase in the forward cross section and skewed shape (not symmetric about 90°) due to significant contributions from nonresonant T matrices (of symmetry other than Π_g).

Equally good agreement is apparent in Fig. 6(c), where we compare elastic DCSs at the third elastic peak which occurs at 2.46 eV in both the experimental and theoretical results. At an energy so near the middle of the resonance region, one might naively expect the resonant Π_g symmetry to dominate the elastic cross section, as it does the inelastic cross sections of Fig. 5(c). But the shape of the DCS in Fig. 6(c) shows that this DCS only weakly manifests the resonant symmetry—a conclusion borne out by symmetry studies like that of Fig. 3(b), which show the importance of nonresonant symmetries at this energy. Both the present results differ substantially from the DCS of Shyn and Carignan [45], which, although also (notionally) measured at the third peak in the elastic cross section, is lower than both present results at all angles and lacks the oscillations near 90°.

Finally, in Fig. 6(d) we show the elastic DCS at the third peak *in the 0→1 inelastic DCS.* This peak occurs at 2.61 eV in the excitation function and quite nearby, at 2.60 eV, in the theoretical DCS, i.e., about 150 meV higher than the energies of Fig. 6(b). This comparison, then, corresponds roughly to the valley between the third and the fourth peaks in the elastic cross section and so, like that in Fig. 6(b), is off peak in this channel. Both DCSs in Fig. 6(d) vary smoothly and show little trace of the characteristic angular Π_g dependence so evident at lower energies [see Figs. 6(a) and 6(b)]. The major

TABLE III. Theoretical resonant elastic ($0 \rightarrow 0$) and inelastic ($0 \rightarrow 1$) differential cross sections for e-N_2 scattering (10^{-16} cm^2 sr^{-1}) at incident energies chosen with reference to structures in the *calculated DCSs* at 60°.

Angle	$v_0=0 \rightarrow v=1$			$v_0=0 \rightarrow v=0$			
(deg)	1.95 eV	2.46 eV	2.60 eV	1.90 eV	1.95 eV	2.46 eV	2.60 eV
0.0	1.016	0.276	1.015	2.106	2.575	5.745	2.666
5.0	0.998	0.271	0.998	2.049	2.521	5.656	2.656
10.0	0.945	0.259	0.948	1.899	2.376	5.407	2.632
15.0	0.862	0.238	0.869	1.699	2.180	5.038	2.599
20.0	0.757	0.211	0.767	1.501	1.975	4.597	2.551
25.0	0.641	0.179	0.651	1.337	1.786	4.117	2.477
30.0	0.524	0.146	0.532	1.220	1.626	3.626	2.361
35.0	0.415	0.116	0.421	1.150	1.497	3.146	2.202
40.0	0.324	0.090	0.328	1.123	1.399	2.703	2.010
45.0	0.256	0.070	0.258	1.136	1.335	2.322	1.805
50.0	0.215	0.059	0.215	1.187	1.308	2.023	1.605
55.0	0.201	0.054	0.198	1.271	1.316	1.812	1.423
60.0	0.211	0.056	0.206	1.377	1.353	1.683	1.264
65.0	0.240	0.063	0.232	1.490	1.404	1.620	1.128
70.0	0.278	0.073	0.269	1.593	1.456	1.600	1.012
75.0	0.320	0.084	0.309	1.672	1.496	1.599	0.915
80.0	0.356	0.094	0.345	1.716	1.513	1.596	0.834
85.0	0.381	0.101	0.371	1.720	1.502	1.574	0.766
90.0	0.389	0.104	0.381	1.681	1.459	1.524	0.709
95.0	0.380	0.103	0.374	1.601	1.386	1.443	0.662
100.0	0.356	0.097	0.351	1.488	1.291	1.341	0.627
105.0	0.319	0.088	0.317	1.355	1.186	1.233	0.608
110.0	0.278	0.077	0.277	1.218	1.083	1.142	0.608
115.0	0.239	0.067	0.240	1.091	0.998	1.095	0.631
120.0	0.211	0.059	0.212	0.988	0.943	1.113	0.681
125.0	0.201	0.056	0.202	0.922	0.930	1.218	0.761
130.0	0.216	0.059	0.215	0.900	0.964	1.423	0.870
135.0	0.257	0.069	0.254	0.929	1.050	1.734	1.010
140.0	0.325	0.086	0.320	1.007	1.187	2.143	1.175
145.0	0.418	0.109	0.408	1.129	1.366	2.634	1.361
150.0	0.527	0.137	0.514	1.283	1.575	3.177	1.559
155.0	0.645	0.167	0.628	1.455	1.797	3.737	1.756
160.0	0.762	0.197	0.740	1.629	2.015	4.273	1.941
165.0	0.867	0.224	0.842	1.787	2.210	4.743	2.100
170.0	0.949	0.245	0.922	1.915	2.364	5.111	2.223
175.0	1.003	0.259	0.973	1.998	2.464	5.345	2.300
180.0	1.021	0.264	0.991	2.027	2.498	5.425	2.327

difference between the experimental and the theoretical DCSs—the former manifests a shallower minimum than the latter—may be due to the finite energy resolution of the measurements.

C. Nonresonant elastic scattering

Comparison of experimental and theoretical DCSs below and above the resonance region requires no special protocol and reveals fascinating features. We begin with three energies below the resonance (0.55, 1.0, and 1.5 eV), then turn to six above it (4.0, 5.0, 6.0, 7.0, 8.0, and 10.0 eV)—energies chosen in part to facilitate comparison to the several other measured and calculated elastic e-N_2 DCSs in the literature. Our results at below-resonance energies appear in Tables IV and V.

Figure 7(a) compares the present elastic DCSs at our lowest energy, 0.55 eV, with those from previous measurements by Sohn *et al.* [54] and by Shi, Stephen, and Burrow [58]. Agreement between the present experimental and theoretical results is generally good. The agreement between our DCS and that of Shi, Stephen, and Burrow [58] is also encouraging, with points across the entire angular range lying well within the overlap of uncertainties. The results of Sohn *et al.* [54] are uniformly lower than ours by about 20%; moreover, these authors predict a decrease in the DCS at scattering angles above 120° that is not present in other experimental DCSs and in the theoretical cross sections appears only weakly and at larger angles. More interesting differences appear in

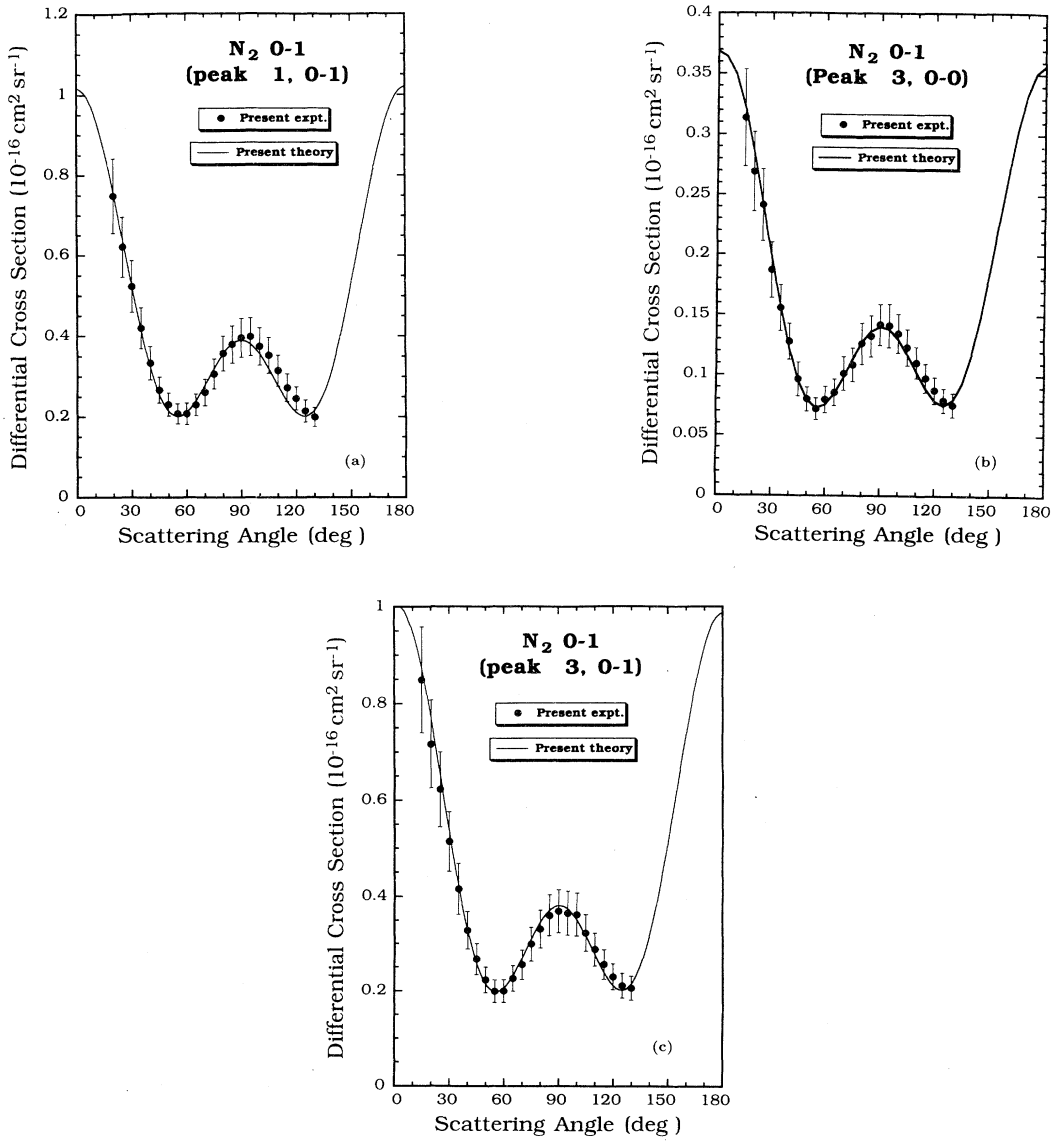

FIG. 5. Absolute DCS for vibrational excitation of N_2 at the position of (a) the first resonance peak in the $0\rightarrow1$ channel, (b) the third resonance peak in the $0\rightarrow0$ channel, and (c) the third resonance peak in the $0\rightarrow1$ channel, all determined at 60°: theoretical DCSs (solid line), measured DCSs (closed circles).

the 1.0-eV DCS in Fig. 7(b). The present experimental and theoretical results have nearly the same shape and both show a maximum near 100°. But, except in the vicinity of this maximum, the two DCSs appear out of phase by about 10°. The experimental results of Sohn *et al.* are again uniformly lower than our DCS by about 20–30 %.

The most extensively studied energy for elastic e-N_2 scattering is 1.5 eV. Previous measurements include those by Shyn and Carignan [45], Sohn *et al.* [54], Brennan *et al.* [57], and Shi, Stephen, and Burrow [58]; previous calculations include hybrid-theory calculations by Chandra and Temkin [34], Schwinger multichannel calculations by Huo *et al.* [30], and rigid-rotor calculations by Morrison, Saha, and Gibson [61]. Indeed, the lack of agreement at this energy between previous experimental and theoretical DCSs motivated (in part) the recent experimental investigations of Brennan *et al.*, Shi, Stephen, and Burrow, and the present work.

Regrettably, as Fig. 7(c) indicates, the outcome of this recent flurry of measurements remains inconclusive. It is apparent that, while the measured DCSs of both Brennan *et al.* and Shi, Stephen, and Burrow are in rough agreement as to the absolute magnitude of the peak at intermediate angles, there remain substantial systematic discrepancies between them. The measurements of Bren-

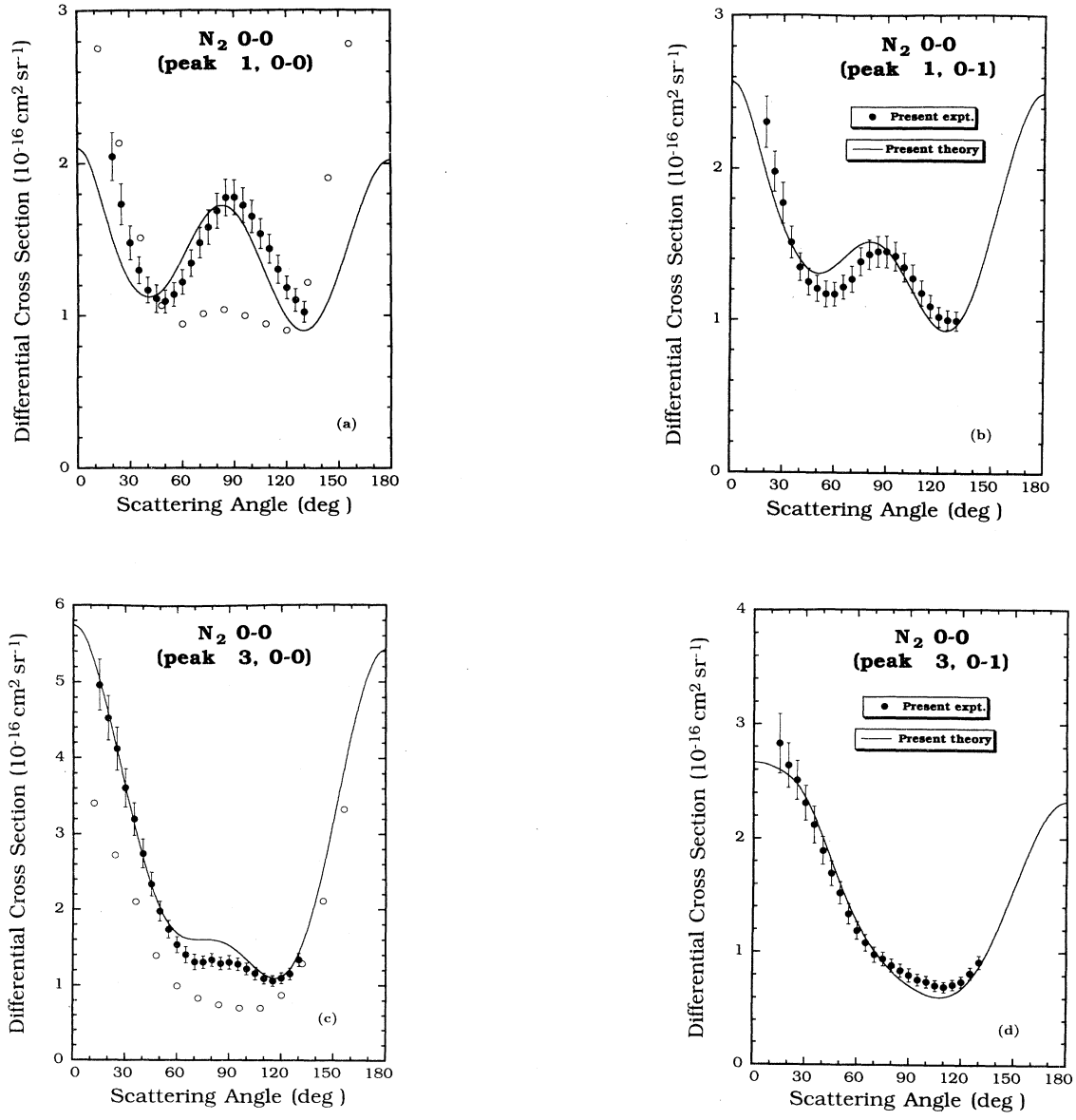

FIG. 6. Absolute elastic differential cross section for e-N_2 scattering at energies corresponding to (a) the first resonance peak in the $0\rightarrow 0$ channel, (b) the first resonance peak in the $0\rightarrow 1$ channel, (c) the third resonance peak in the $0\rightarrow 0$ channel, and (d) the third resonance peak in the $0\rightarrow 1$ channel, all as determined at a scattering angle of 60°. In addition to the present experimental (solid circles) and theoretical (solid lines) results, we show in (a) and (c) the measured DCS of Shyn and Carignan [45] (open circles).

nan *et al.* were taken on the same apparatus used in the present study, although as discussed in Sec. II, in those earlier experiments the relative flow technique was applied in a fashion we now consider to be less accurate than the one used here. Still, we consider the differences near the maximum of the DCS in Fig. 7(c) to be greater than we would expect in absolute measurements of nonresonant cross sections. As at 1.0 eV, in Fig. 7(c) at 1.5 eV we find the present experimental and theoretical results to be out of phase by about 10°. The present results support the conclusions of Brennan *et al.* and Shi, Stephen, and Burrow that the absolute magnitudes of the elastic cross sections reported by Shyn and Carignan and Sohn *et al.* are too low.

The totality of theoretical data at this energy provides little further clarification. As at 1.0 eV in Fig. 7(b), the present theoretical DCS at 1.5 eV agrees better with the present measured data at angles above about 110° than at smaller angles, where it is slightly higher. The calculated cross section of Huo *et al.*, however, agree best with our measured data at precisely these smaller angles, while the DCS of Chandra and Temkin overestimates this cross section at all but the largest angles.

Turning now to energies above the resonance, we have measured and calculated the elastic DCSs on a relatively fine energy grid (see Tables VI and VII) in order to track a fascinating feature that develops at small angles. This feature first appears at the high end of the resonance re-

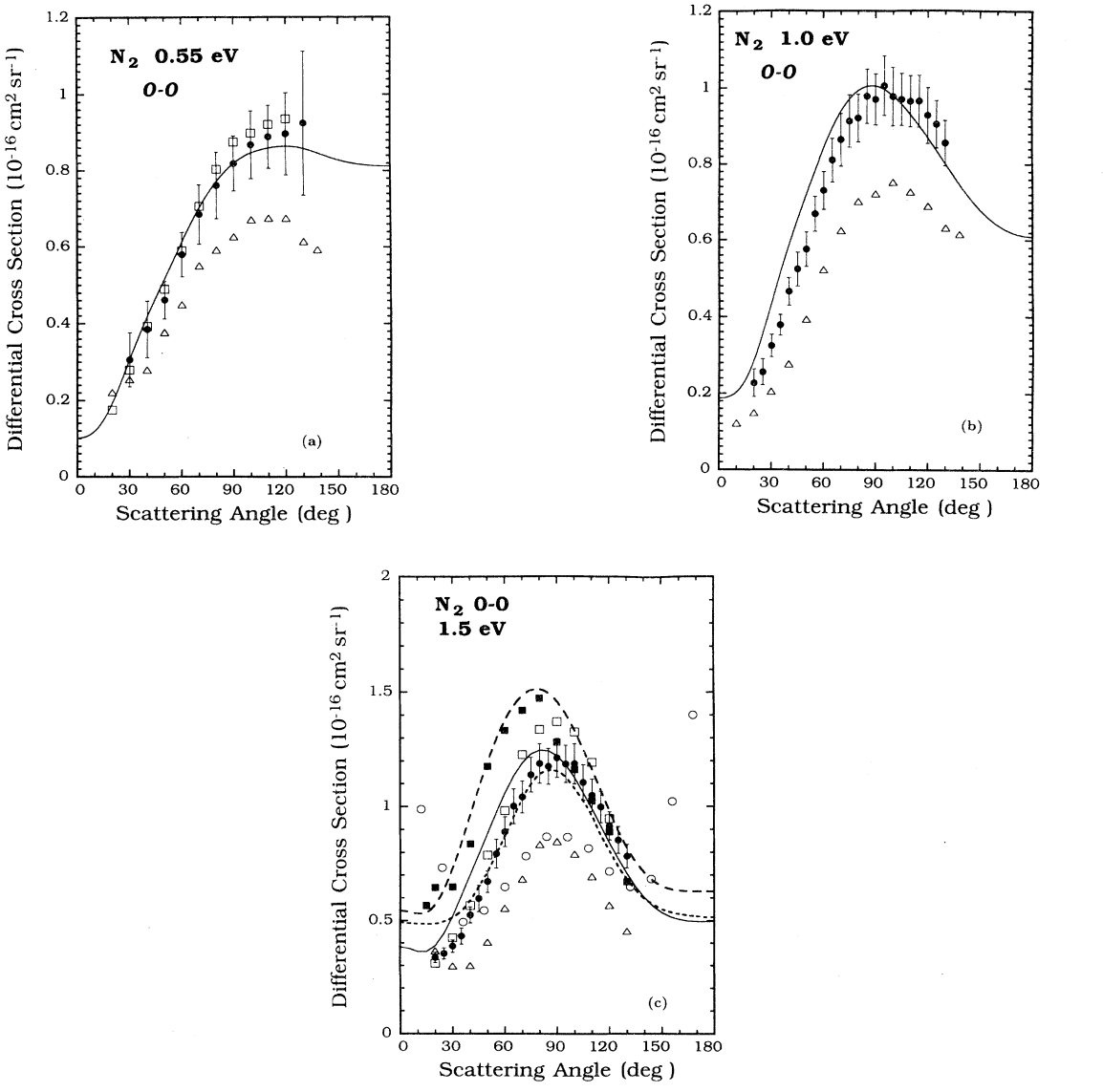

FIG. 7. Absolute elastic differential cross sections at energies of (a) 0.55 eV, (b) 1.0 eV, and (c) 1.5 eV. In addition to the present experimental (solid circles) and theoretical (solid lines) results, we show the data of Sohn *et al.* [54] (open triangles) and in (a) and (c) of Shi, Stephen, and Burrow [58] (open squares). Also shown in (c) are measured DCSs of Shyn and Carignan [45] (open circles) and the hybrid-theory results of Chandra and Temkin [34] (long-dashed line) and Schwinger multichannel DCSs of Huo *et al.* [30] (short-dashed line).

gion, in the 4.0-eV DCS in Fig. 8(a). Both the experimental and theoretical results at this energy exhibit a maximum at about 30°. As noted in regard to Fig. 3(c), this small-angle feature arises from long-range scattering in high-order partial waves: only when we complete the sums in Eq. (3) to convergence does it appear. Although the small-angle theoretical DCS exceeds the present experimental data (as well as that of Shyn and Carignan), at higher angles agreement between the present experimental and theoretical DCSs is excellent.

The most extensively studied above-resonance e-N_2 DCS is that at 5.0 eV. In Fig. 8(b) we compare our results at this energy with prior results measured by Srivastava, Chutjian, and Trajmar [41] and Brennan *et al.* [57] as well as DCSs calculated in previous theoretical determinations. The present experimental data agree with that of Brennan *et al.* except at small angles, where the earlier results are larger by about 20%, and with that of Shyn and Carignan except at the largest (common) angles, where the latter is also larger. The DCS of Srivastava, Chutjian, and Trajmar, however, is uniformly smaller than the present data at all scattering angles.

As at 4.0 eV, the present theoretical 5.0-eV DCSs agree very well with the present experimental points above the maximum. Indeed, all the theoretical calculations, except the R-matrix study of Gillan *et al.* [28], yield DCSs that exhibit the experimentally observed maximum at roughly 30°. But only the Schwinger multichannel DCSs of Huo *et al.* [30] agree in magnitude with our experimental data at small angles. These Schwinger results begin to deviate from these data above about 100°, where they show an angular dependence not seen in any other results. In shape, the hybrid-theory DCS of Chandra and Temkin agrees well with the present results, but in magnitude they are uniformly 30–50 % higher.

As the energy increases above 5.0 eV, the small-angle maximum in the elastic DCS gradually flattens out and then begins to increase. This trend is evident in the DCSs at 6.0, 7.0, 8.0, and 10 eV, shown in Figs. 8(c)–8(f). Throughout this energy range the theoretical small-angle DCSs remain larger than the experimental points but exhibit the same structural development.

At 7.0 eV, where data from previous experiments are available, we see in Fig. 8(d) that below 40°, our measured DCSs are systematically lower than those of Srivastava, Chutjian, and Trajmar and Shyn and Carignan, but our calculated DCSs are in better agreement with data from these two prior determinations than from the present measurements. Srivastava, Chutjian, and Trajmar used

TABLE IV. Experimental elastic (0→0) differential cross sections for e-N_2 scattering (10^{-16} cm^2 sr^{-1}) at incident energies below the resonance region.

Angle (deg)	0.55 eV	1.0 eV	1.5 eV
20.0		0.227	0.336
25.0		0.256	0.354
30.0	0.306	0.324	0.386
35.0		0.378	0.432
40.0	0.385	0.466	0.525
45.0		0.524	0.597
50.0	0.461	0.576	0.670
55.0		0.669	0.794
60.0	0.580	0.731	0.890
65.0		0.811	1.001
70.0	0.685	0.864	1.041
75.0		0.913	1.139
80.0	0.761	0.921	1.188
85.0		0.978	1.176
90.0	0.819	0.970	1.213
95.0		1.006	1.186
100.0	0.868	0.978	1.187
105.0		0.970	1.105
110.0	0.888	0.965	1.048
115.0		0.965	0.997
120.0	0.896	0.928	0.914
125.0		0.905	0.853
130.0	0.924	0.856	0.782

TABLE V. Theoretical elastic (0→0) differential cross sections for e-N_2 scattering (10^{-16} cm^2 sr^{-1}) at incident energies below the resonance region.

Angle (deg)	0.55 eV	1.0 eV	1.5 eV
0.0	0.101	0.187	0.383
5.0	0.105	0.190	0.376
10.0	0.120	0.203	0.363
15.0	0.149	0.234	0.362
20.0	0.193	0.286	0.388
25.0	0.248	0.356	0.443
30.0	0.307	0.435	0.521
35.0	0.365	0.513	0.609
40.0	0.418	0.587	0.701
45.0	0.468	0.655	0.792
50.0	0.516	0.720	0.884
55.0	0.565	0.783	0.974
60.0	0.613	0.842	1.059
65.0	0.660	0.895	1.133
70.0	0.702	0.938	1.191
75.0	0.739	0.971	1.230
80.0	0.771	0.993	1.248
85.0	0.798	1.005	1.245
90.0	0.819	1.006	1.222
95.0	0.835	0.997	1.182
100.0	0.846	0.980	1.126
105.0	0.854	0.957	1.060
110.0	0.859	0.930	0.988
115.0	0.862	0.901	0.914
120.0	0.864	0.870	0.840
125.0	0.862	0.836	0.770
130.0	0.858	0.802	0.706
135.0	0.851	0.767	0.648
140.0	0.843	0.734	0.601
145.0	0.835	0.703	0.563
150.0	0.828	0.677	0.535
155.0	0.823	0.655	0.516
160.0	0.818	0.638	0.505
165.0	0.815	0.625	0.499
170.0	0.813	0.616	0.497
175.0	0.813	0.611	0.497
180.0	0.812	0.609	0.497

the relative flow technique with their own *e*-He cross section to determine the absolute elastic *e*-N_2 DCS. Repeating their determination using instead the theoretical *e*-He cross sections of Nesbet [62] as the reference standard (as in the present experiment) reduces the forward-scattering cross section by about 10%, but does not significantly affect the comparison. Here, as at other above-resonance energies, the present theoretical DCSs agree with experiment except at small angles. We do consider the qualitative differences evident in this figure to be significant: the present measured DCSs assume an essentially constant value about 30–40 % lower than the values predicted by other experiments, which do not show a maximum, while the maximum in our theoretical DCS remains strong.

By 8.0 eV, as shown in Fig. 8(e), the experimental elastic DCS at forward angles rises rather steadily through a broad shoulder at around 40°, behavior quite different from that seen at 4.0 eV in Fig. 8(a). Finally in the 10.0-eV DCS in Fig. 8(f), the small-angle maximum has disappeared from the measured data and is all but absent from the theoretical result. At this energy we can again compare with prior experimental results. We find good agreement between the present measured DCS and those of both Srivastava, Chutjian, and Trajmar and Shyn and Carignan at angles above about 50° but not below. The present theoretical results at small angles agree best with those of these two earlier experiments, but at large angles do not show the marked rise evident in their data.

VII. RESULTS: INTEGRAL CROSS SECTIONS

The present study provides information on a number of integral cross sections, including the grand total cross section as measured with the TOF spectrometer, the total cross sections for elastic scattering and 0→1 vibrational excitation as derived from the DCS measurements, and all of these cross sections as calculated within the theoretical context described in Sec. III. Moreover, one can use the adiabatic-nuclear-rotation theory to extract from total vibrationally inelastic cross sections in the resonance region any desired rovibrational ICS or DCS as a function of energy at any desired angle [107]. Determining these total ICSs from the normalized angular distributions measured in the crossed beam experiments, however, requires extrapolation of these data to 0° and 180° and subsequent numerical integration, a procedure that in the past has introduced significant additional error into the ICS beyond that inherent in the angular distributions. We have implemented a physically based phase-fitting procedure that eliminates most of this additional error; this procedure is described in Sec. VII A, following which we present and compare to prior studies our measured and calculated ICSs in Sec. VII B.

A. Determination of electron-molecule ICSs from measured angular distributions

To facilitate comparison of measured angular distributions with ICSs from other experiments and theory, we require the DCS over the entire angular range. We have designed an extrapolation procedure for producing such ICSs by a nonlinear least-squares fit to the measured angular distributions using the following guidelines: (i) the fitting equations should reflect known physical properties of the system and its S matrix but (ii) should be indepen-

TABLE VI. Experimental elastic (0→0) differential cross sections for *e*-N_2 scattering (10^{-16} $cm^2\,sr^{-1}$) at incident energies above the resonance region.

Angle (deg)	4.0 eV	5.0 eV	6.0 eV	7.0 eV	8.0 eV	10.0 eV
15.0	1.613		1.481	1.565	1.719	2.342
20.0	1.705	1.572	1.495	1.552	1.641	2.036
25.0	1.781	1.605	1.547	1.572	1.603	1.875
30.0	1.782	1.617	1.567	1.557	1.564	1.774
35.0	1.742	1.678	1.582	1.567	1.535	1.654
40.0	1.686	1.599	1.557	1.540	1.484	1.587
45.0	1.625	1.509	1.510	1.452	1.442	1.454
50.0	1.521	1.400	1.417	1.357	1.357	1.299
55.0	1.405	1.291	1.305	1.221	1.262	1.154
60.0	1.239	1.115	1.200	1.101	1.133	0.990
65.0	1.138	0.998	1.051	0.954	1.000	0.842
70.0	0.986	0.882	0.926	0.847	0.858	0.704
75.0	0.878	0.789	0.800	0.714	0.693	0.573
80.0	0.784	0.704	0.705	0.647	0.607	0.471
85.0	0.697	0.649	0.629	0.559	0.529	0.402
90.0	0.649	0.600	0.565	0.512	0.472	0.354
95.0	0.625	0.551	0.522	0.480	0.436	0.351
100.0	0.609	0.543	0.516	0.465	0.433	0.352
105.0	0.608	0.520	0.513	0.462	0.438	0.378
110.0	0.586	0.521	0.508	0.469	0.448	0.410
115.0	0.594	0.527	0.520	0.492	0.492	0.465
120.0	0.601	0.536	0.534	0.514	0.511	0.515
125.0	0.606	0.551	0.540	0.535	0.551	0.561
130.0	0.634	0.558	0.570	0.568	0.588	0.609

dent of particular theoretical calculations, which bring into play a host of additional assumptions (see Sec. III). This philosophy underlies the widely used phase-shift analysis methods of electron-atom scattering [108,109], but as those methods are appropriate to spherically symmetric potentials, they are incorrect for electron-molecule systems.

Our method is based on the equation for the DCS in the BF FNO theory described in Sec. III, i.e., Eq. (1) with expansion coefficients (3). In formulating the fitting equations we must identify the "free parameters" that will vary in order to fit the measured angular distribution data in the DCS equation (1). Consistent with our philosophy of constraining the fit as much as possible, we seek the smallest number of free parameters that allows sufficient flexibility to fit the data. To this end we use the first Born approximation expressions (18) for high-order partial waves as described below.

The dynamical information is contained entirely in the T-matrix elements in Eq. (3). But these elements themselves are not convenient as parameters: they are complex, so each element would lead to two real parameters. We choose instead the K matrix of Eq. (12), the elements of which are easily parametrized in terms of the "phase parameters" δ_l^A defined by

$$K_{l,l}^{\Lambda} \equiv \tan\delta_l^{\Lambda} \ . \tag{24}$$

Since the K matrix is real and symmetric, the corresponding S matrix is guaranteed to be unitary. Since we seek to determine only elastic ICSs, we do not allow flux to leave the elastic channel; although this approximation is satisfactory over the energy range of the present study to within the accuracy of the raw data, it would have to be checked for other systems.

As noted in Sec. III, the number of K-matrix elements that contributes to the DCS may be large, and to allow all such elements to be free parameters would lead to a

TABLE VII. Theoretical elastic (0→0) differential cross sections for e-N_2 scattering (10^{-16} $cm^2\,sr^{-1}$) at incident energies above the resonance region.

Angle (deg)	4.0 eV	5.0 eV	6.0 eV	7.0 eV	8.0 eV	10.0 eV
0.0	2.390	1.980	1.939	2.015	2.140	2.460
5.0	2.414	2.003	1.955	2.022	2.136	2.432
10.0	2.482	2.071	2.007	2.052	2.139	2.371
15.0	2.577	2.178	2.098	2.118	2.174	2.328
20.0	2.668	2.296	2.210	2.210	2.238	2.323
25.0	2.709	2.382	2.298	2.286	2.296	2.329
30.0	2.668	2.394	2.320	2.303	2.300	2.297
35.0	2.535	2.320	2.258	2.237	2.225	2.195
40.0	2.330	2.170	2.119	2.096	2.075	2.025
45.0	2.085	1.973	1.931	1.903	1.874	1.807
50.0	1.829	1.755	1.719	1.686	1.650	1.567
55.0	1.583	1.538	1.503	1.465	1.422	1.327
60.0	1.359	1.332	1.297	1.254	1.204	1.100
65.0	1.163	1.146	1.109	1.060	1.006	0.897
70.0	1.000	0.986	0.945	0.892	0.836	0.726
75.0	0.870	0.854	0.810	0.756	0.699	0.593
80.0	0.772	0.752	0.706	0.653	0.599	0.501
85.0	0.702	0.678	0.632	0.582	0.533	0.448
90.0	0.656	0.629	0.585	0.540	0.499	0.430
95.0	0.628	0.599	0.560	0.523	0.491	0.440
100.0	0.614	0.585	0.552	0.524	0.502	0.470
105.0	0.611	0.583	0.556	0.538	0.525	0.511
110.0	0.617	0.587	0.567	0.557	0.554	0.555
115.0	0.631	0.595	0.580	0.578	0.581	0.595
120.0	0.653	0.606	0.593	0.596	0.605	0.628
125.0	0.684	0.618	0.605	0.611	0.624	0.652
130.0	0.725	0.633	0.616	0.624	0.639	0.669
135.0	0.777	0.651	0.628	0.635	0.650	0.681
140.0	0.841	0.673	0.640	0.644	0.659	0.689
145.0	0.915	0.699	0.653	0.654	0.666	0.695
150.0	0.996	0.728	0.668	0.662	0.672	0.698
155.0	1.079	0.758	0.683	0.671	0.677	0.699
160.0	1.159	0.787	0.697	0.678	0.680	0.700
165.0	1.229	0.813	0.709	0.685	0.684	0.701
170.0	1.282	0.833	0.718	0.689	0.686	0.702
175.0	1.316	0.845	0.724	0.793	0.688	0.703
180.0	1.327	0.850	0.726	0.694	0.688	0.703

severely underconstrained fit. So we incorporate into this procedure the fact that *most* of these elements, in particular, diagonal elements with high partial-wave order and all non-negligible off-diagonal elements, are accurately given in the first Born approximation. So although these high-order and off-diagonal elements are extremely important to determining the shape of the DCS (especially at low angles), their inclusion via the FBA is trivial. For e-N_2 scattering, only off-diagonal elements with $|\Delta l \equiv l - l_0| = 2$ contribute appreciably to the DCS coefficients (3), and we set all other such elements to zero. The fit, then, must determine only a few free parameters, those corresponding to low-order partial waves. Further details of this analysis may be found in a forthcoming paper [110].

Under these assumptions and with the parametrization (24), the fitted K matrix in each symmetry assumes a form illustrated here by the Σ_g symmetry with two free parameters:

$$\mathsf{K}^{\Sigma_g} = \begin{bmatrix} \tan\delta_0^{\Sigma_g} & K_{0,2}^{(\mathrm{FBA})} & 0 & \cdots \\ K_{2,0}^{(\mathrm{FBA})} & \tan\delta_2^{\Sigma_g} & K_{2,4}^{(\mathrm{FBA})} & 0 \\ 0 & K_{4,2}^{(\mathrm{FBA})} & K_{4,4}^{(\mathrm{FBA})} & K_{4,6}^{(\mathrm{FBA})} \\ 0 & & \ddots & \ddots \end{bmatrix} . \tag{25}$$

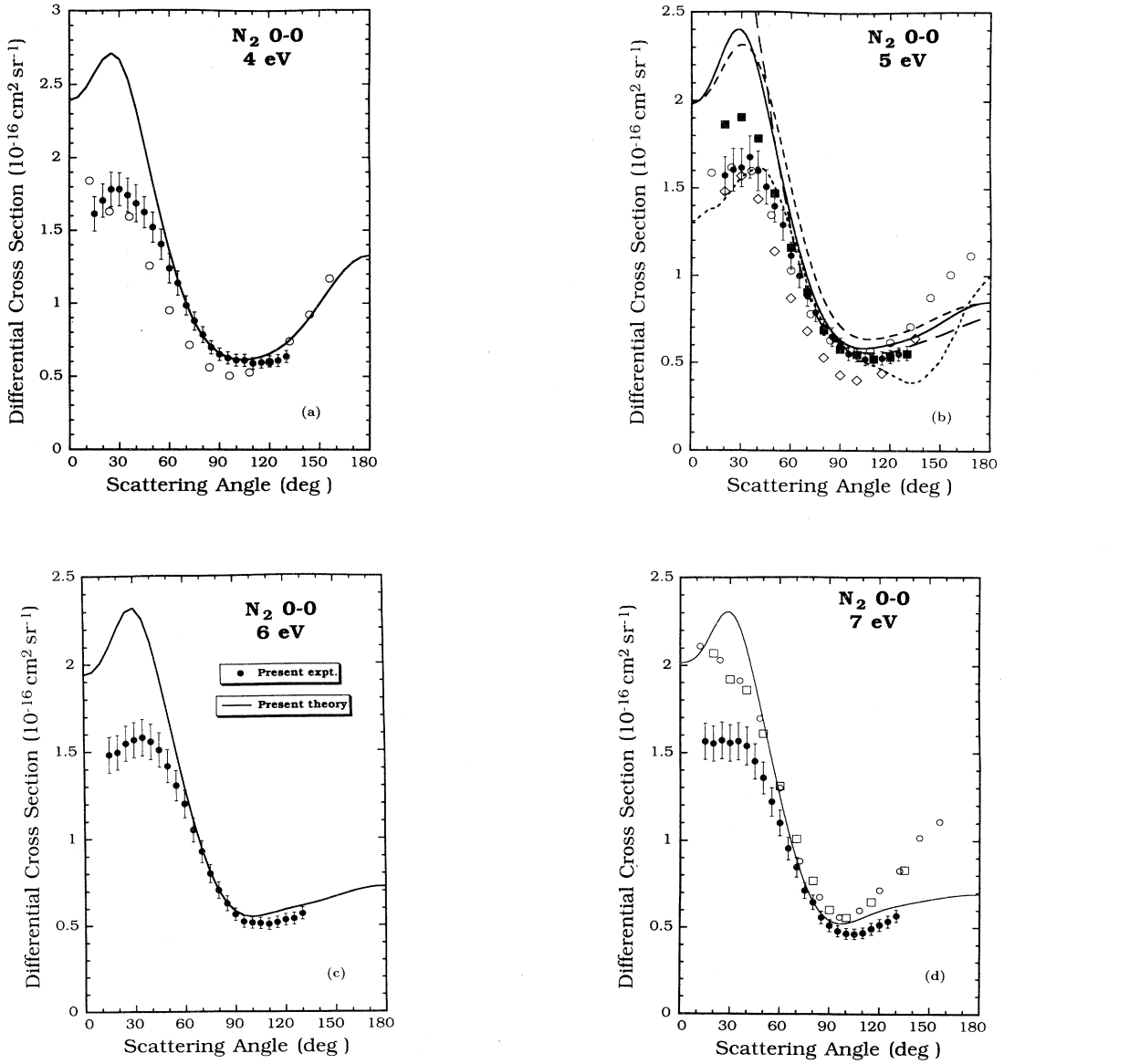

FIG. 8. Absolute elastic differential cross sections at energies of (a) 4.0 eV, (b) 5.0 eV, (c) 6.0 eV, (d) 7.0 eV, (e) 8.0 eV, and (f) 10 eV. In addition to the present experimental (solid circles) and theoretical (solid lines) results, we also show in (a), (b), (d), and (f) the measured DCSs of Shyn and Carignan [45] (open circles), in (b), (d), and (f) the results of Srivastava, Chutjian, and Trajmar [41] (open diamonds), and in (b) measured data of Brennan *et al.* [57] (closed squares) and theoretical results from hybrid-theory calculations by Chandra and Temkin [34] (medium-dashed line), Schwinger multichannel DCSs of Huo *et al.* [30] (short-dashed line), and R-matrix calculations of Gillan *et al.* [28] (long-dashed line).

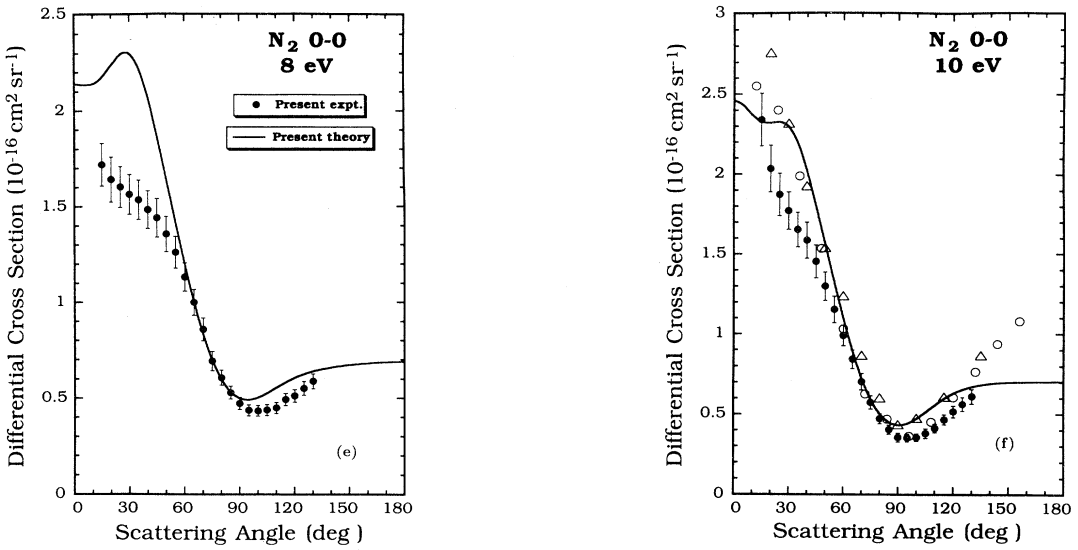

FIG. 8. (*Continued*).

This procedure differs significantly in implementation from our original version, as described by Crompton and Morrison [111] in a study of e-H_2 scattering. That earlier implementation, which was more directly based on Eq. (3), did not allow easy incorporation of off-diagonal T-matrix elements. Such elements are unimportant for low-energy e-H_2 collisions, but vital for e-N_2 scattering.

Operationally, we determine the free parameters using the Levenberg-Marquardt nonlinear least-squares fit [112]. As a measure of the quality of the fit we have adopted the usual definition of the reduced χ^2 function [75]. Thus a value of χ^2 near 1 indicates that the model and the data (with the given error estimates) are consistent. In Fig. 9 we demonstrate the fitting procedure

TABLE VIII. Elastic integral and momentum transfer cross sections (10^{-16} cm^2 sr^{-1}) for e-N_2 scattering. The "fitted" cross sections were determined from measured angular distributions using the procedure described in the indicated free parameters. The reduced chi square for each fit is given as χ^2.

	Free		$\sigma^{(v)}_{0\to 0}$		$\sigma^{(m)}$	
E (eV)	parameters	χ^2	Fitted	Theory	Fitted	Theory
0.55	$\delta_0^{\Sigma_g},\delta_1^{\Sigma_u},\delta_1^{\Pi_u}$	0.107	9.12	8.8928	10.68	10.1048
1.0	$\delta_0^{\Sigma_g},\delta_1^{\Sigma_u},\delta_1^{\Pi_u},\delta_2^{\Pi_g}$	0.073	9.84	10.1186	10.78	10.5726
1.5	$\delta_0^{\Sigma_g},\delta_1^{\Sigma_u},\delta_1^{\Pi_u},\delta_2^{\Pi_g}$	0.090	10.83	11.2967	11.12	11.0233
1.92[a]	$\delta_0^{\Sigma_g},\delta_1^{\Sigma_u},\delta_1^{\Pi_u},\delta_2^{\Pi_g}$	0.047	18.00	17.0401	17.40	16.5394
1.98[b]	$\delta_0^{\Sigma_g},\delta_1^{\Sigma_u},\delta_1^{\Pi_u},\delta_2^{\Pi_g}$	0.926	17.93	17.3932	18.03	16.7119
2.46	$\delta_0^{\Sigma_g},\delta_1^{\Sigma_u},\delta_1^{\Pi_u},\delta_2^{\Pi_g}$	0.827	21.10	25.8745	16.65	24.3806
2.605[c]	$\delta_0^{\Sigma_g},\delta_1^{\Sigma_u},\delta_3^{\Sigma_u},\delta_1^{\Pi_u},\delta_2^{\Pi_g}$	0.452	14.78	15.0368	12.38	13.0533
4.0	$\delta_0^{\Sigma_g},\delta_1^{\Sigma_u},\delta_1^{\Pi_u},\delta_2^{\Pi_g}$	0.088	12.01	14.3925	9.64	10.9250
5.0	$\delta_0^{\Sigma_g},\delta_1^{\Sigma_u},\delta_1^{\Pi_u},\delta_2^{\Pi_g}$	0.033	10.90	13.0709	8.64	9.5663
6.0	$\delta_0^{\Sigma_g},\delta_1^{\Sigma_u},\delta_1^{\Pi_u},\delta_2^{\Pi_g}$	0.156	10.69	12.5510	8.29	9.0816
7.0	$\delta_0^{\Sigma_g},\delta_1^{\Sigma_u},\delta_3^{\Sigma_u},\delta_1^{\Pi_u},\delta_2^{\Pi_g}$	0.070	10.44	12.2596	8.31	8.8525
8.0	$\delta_0^{\Sigma_g},\delta_1^{\Sigma_u},\delta_3^{\Sigma_u},\delta_1^{\Pi_u},\delta_2^{\Pi_g}$	0.114	10.60	12.0432	8.53	8.7124
10.0	$\delta_0^{\Sigma_g},\delta_1^{\Sigma_u},\delta_3^{\Sigma_u},\delta_1^{\Pi_u},\delta_2^{\Pi_g}$	0.352	10.55	11.6851	8.40	8.5161

[a]First peak in the 0→0 DCS at 60°; the theoretical energy is equal to 1.90 eV.
[b]Third peak in the 0→1 DCS at 60°; the theoretical energy is equal to 1.95 eV.
[c]Third peak in the 0→1 DCS at 60°; the theoretical energy is equal to 2.60 eV.

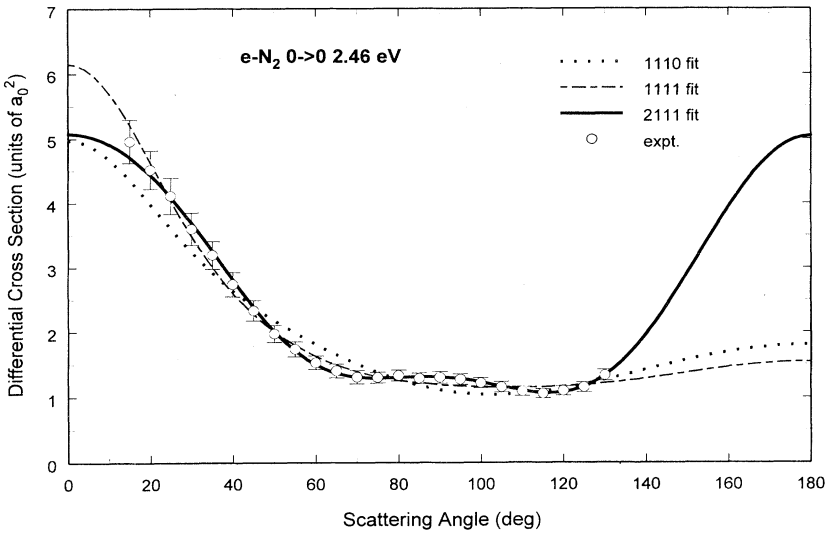

FIG. 9. Fits to measured e-N_2 angular distributions (open circles with error bars) at 2.46 eV, the third resonant peak of the experimental elastic DCSs at 60°. The fitted DCSs are converged in asymptotic partial waves and symmetries with the indicated parameters left free.

for the measured e-N_2 DCS at 2.46 eV, the energy of the third resonance peak in the elastic angular distribution. At this energy, it is essential to allow the two d-wave parameters $\delta_2^{\Sigma_g}$ and $\delta_2^{\Pi_g}$ to be free so the fit can reproduce the rather subtle angular variation between 45° and 135°. At small angles, the inclusion of high-order asymptotic partial waves and symmetries as described in Sec. IV is essential. The elastic integral and momentum-transfer

TABLE IX. Experimental and theoretical grand total cross sections for e-N_2 scattering (10^{-16} cm^{-2}sr^{-1}) at selected nonresonance incident energies (eV).

Energy	Theory	Experiment
0.02	2.568	
0.04	3.351	
0.06	3.951	
0.08	4.452	4.468
0.10	4.883	4.771
0.12	5.261	4.960
0.14	5.598	5.324
0.16	5.902	5.562
0.18	6.178	5.858
0.20	6.431	6.098
0.35	7.816	7.740
0.55	8.893	8.758
0.70	9.415	9.123
0.80	9.685	9.324
1.00	10.120	9.734
1.50	11.313	10.910
4.00	14.596	13.391
5.00	13.120	11.812
6.00	12.570	11.442
7.00	12.270	11.196
8.00	12.050	11.111
9.00	11.861	11.325
10.00	11.689	11.818

TABLE X. Experimental and theoretical grand total e-N_2 cross sections (10^{-16} cm^{2}sr^{-1}) in the resonance region. Note that incident energies (in eV) for comparison should be chosen with reference to structure in the *measured excitation function* at 60°.

Theory		Experiment	
Energy	Cross section	Energy	Cross section
1.500	11.313	1.500	10.910
1.600	11.816	1.601	11.772
1.700	12.663	1.704	13.252
1.800	14.357	1.748	14.100
1.850	15.920	1.802	15.802
1.900	18.191	1.850	18.000
1.950	19.549	1.900	21.443
1.980	18.181	1.916	22.830
2.000	16.769	1.925	23.153
2.050	15.055	1.951	25.041
2.100	16.532	1.978	26.103
2.200	26.279	2.005	25.904
2.350	15.811	2.081	23.831
2.400	18.831	2.100	24.390
2.430	23.213	2.151	28.252
2.480	28.730	2.213	33.328
2.500	27.586	2.301	27.728
2.600	16.805	2.335	26.401
2.700	22.311	2.455	32.700
2.730	24.762	2.505	29.756
2.800	22.785	2.598	25.028
2.900	17.325	2.688	28.109
2.950	17.011	2.717	26.936
3.000	18.423	2.746	25.271
3.070	20.322	2.776	23.679
3.200	17.702	2.813	22.649
3.300	16.356	2.860	22.809
3.420	17.013	2.907	23.370
3.500	16.600	2.956	22.329
3.900	14.962	3.006	20.068

ICSs obtained via this procedure at all energies are given along with the theoretical BF FNO cross sections in Table VIII.

B. Experimental and theoretical ICSs

Finally, we turn to the grand total ICS, the sum of cross sections for the elastic and all open inelastic channels. We tabulate this quantity as measured by the TOF apparatus described in Sec. II and as calculated via the theory of Sec. III at nonresonant energies in Table IX and at resonant energies in Table X. These data are compared graphically in Fig. 10 in the three regions of interest—below, in, and above the resonance region—and compared to previously determined data where available.

Throughout the entire energy range below the resonance, Fig. 10(a) shows good agreement between the present TOF and theoretical results, although above 0.7 eV the present TOF data are slightly lower than the

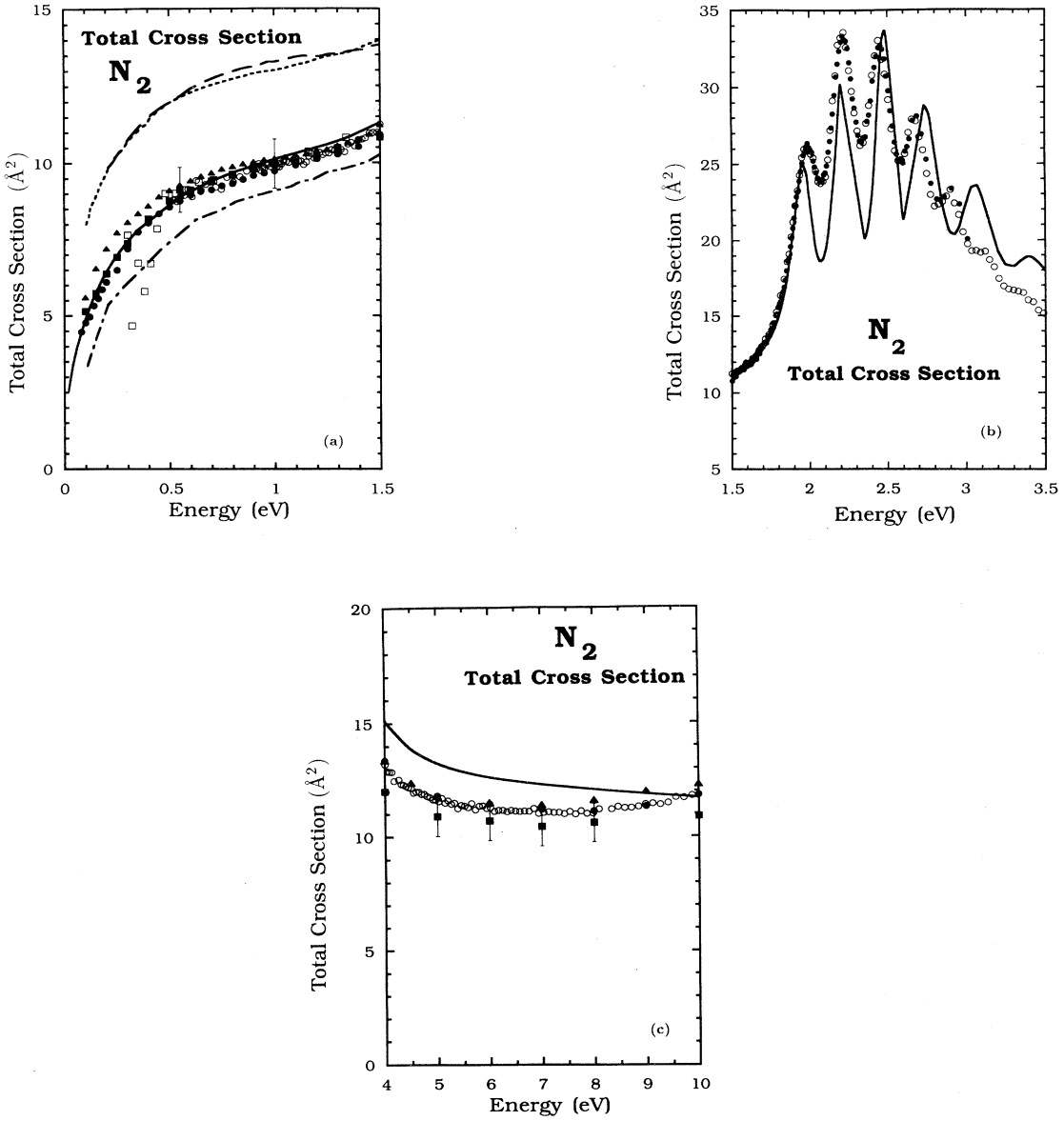

FIG. 10. Absolute grand total cross sections for e-N_2 scattering at energies (a) below 1.5 eV, (b) in the resonance region from 1.5 to 4.0 eV, and (c) from 4 to 10 eV. Experimental data shown include results from the present time-of-flight (solid circles) and crossed-beam (solid squares) experiments as well as measured data by Kennerly [46] (open circles), Ferch, Raith, and Schweiker [55] (solid squares), Jost *et al.* [53] (solid triangles), and Baldwin [40] (open squares). Theoretical results are shown from the present BF FNO calculations (solid curve), R-matrix calculations of Gillan *et al.* [28] (long-dashed line), hybrid-theory calculations by Chandra and Temkin [34] (short-dashed curve), and partial differential equation calculations of Weatherford and Temkin [35] (dot-dashed curve).

theoretical ICSs. We consider the close agreement between the TOF results and the fitted elastic ICSs determined from the measured angular distributions (which at these energies should closely approximate the grand total cross section due to the lack of significant inelastic scattering) particularly significant, considering the quite different nature of these two experimental methods. Turning to other experimental and theoretical results in this energy range, we find best agreement with the TOF data of Kennerly [46] and Ferch, Raith, and Schweiker [55]. Above about 0.7 eV, our TOF data also agree well with those of Baldwin [40] and Jost *et al.* [53], although at the lower end of this energy range both of the latter results differ significantly from the present data.

In the resonance region, as shown in Fig. 10(b), we find excellent agreement between our TOF cross sections and those of Kennerly [46]. Agreement with theory is very good at the lowest few peaks (see Table I), but at higher energies in this region there appears a systematic difference between theory and experiment, the origin of which we do not understand.

Above the resonance region, we compare in Fig. 10(c) various theoretical and experimental grand total ICSs at energies between 4.0 and 10 eV. Once again the agreement between the present TOF data and that of Kennerly [46] is excellent, while both lie below that of Jost *et al.* [53].

The present theoretical ICSs exceed the experimental points below 7.0 eV, as expected from the elastic DCSs, and manifest a different energy dependence above 7 eV. The elastic ICSs derived from the measured elastic angular distributions, which do not account for inelastic scattering, lie below the grand total cross sections throughout this energy range.

VIII. CONCLUSIONS

The present results provide a thorough experimental and theoretical data base for elastic, $0\rightarrow 1$ vibrational, and total e-N_2 cross sections at energies from 0.55 to 10.0 eV. In the theoretical calculations we have emphasized high numerical precision, especially in regard to the important issue of convergence of sums over electron-molecule symmetry classes and asymptotic partial waves as well as a number of vibrational states and partial waves in the near-target expansion of the system wave function. Our theoretical formulation treats exactly (to within our convergence criteria) the coupling of molecular vibrations and the projectile wave function and uses a refined local exchange potential and a well-tested correlation-polarization potential, all based, like the static potential, on a near-Hartree-Fock description of the target. (These simplifications made it possible to perform the entire theoretical study reasonably efficiently on a SparcStation-10 computer workstation.) In the measurements we have used an improved implementation of the relative flow normalization technique and encompassed a more complete range of energies than in our previous work on this system.

A particular focus of this collaboration is the long-standing problem of how to undertake comparisons between results of two experiments (or of experiment and theory) in the resonance region. The central difficulty—the extremely strong energy dependence in both the shape and magnitude of elastic and inelastic cross sections in this region—plagues a number of electron-molecule systems other than e-N_2. We have proposed and demonstrated a general protocol for such comparisons that allows for the frequent disagreement between two data sets on the absolute energies of the important structures that characterize such resonances (see Table I), as a result of which comparisons based directly on energy can be extremely misleading. Instead we compare results at energies determined by their proximity to corresponding well-defined structures in the two data sets. Our development of this protocol also highlights the advantages of collaboration between experiment and theory, as we consider it unlikely that such a scheme would have developed without such detailed interaction.

In general, we consider the comparison between the present experimental and theoretical DCSs extremely encouraging for resonant elastic and inelastic $(0\rightarrow 1)$ scattering. The extreme sensitivity of the resonant DCS to short-range nonlocal and many-body effects (exchange and bound-free correlation) makes the agreement among these DCSs suggestive of the validity of the models we have adopted for these effects. Above and below the resonance, agreement is satisfactory if less compelling. Here we note the centrality of high-order asymptotic partial waves in the construction of the small-angle maximum observed in the measured angular distributions, a feature present in the theoretical results with a magnitude larger than that of the experimental DCS. Interestingly, such small-angle behavior also occurs in other diatomic (e.g., O_2 and NO) and polyatomic (e.g., N_2O) molecules. Although for these systems the quantitative details of this behavior is different from that in e-N_2 scattering, the qualitative similarity (and the aforementioned importance of high-order partial waves) suggests that this feature is primarily due to long-range moments rather than to the intricacies of the nonlocal short-range interactions.

In addition to these DCS determinations we have calculated ICSs from the measured angular distributions using an extension of a previously proposed physically based fitting procedure. The resulting elastic ICSs suffer little more error than the raw (normalized) angular distribution data. These, in turn, we have compared to grand total cross sections measured in a complementary experiment with a TOF apparatus. Although the extensive comparisons presented here indicate a high general level of concordance between experiment and theory, there remain points requiring further effort, especially at the high end of the resonance region.

ACKNOWLEDGMENTS

We would like to acknowledge useful discussions with Dr. Paul Burrow, Dr. Ilya Fabrikant, Dr. Aaron Temkin, and Dr. Mike Brunger concerning various aspects of this work. We would like to thank the technical staff of the

Electron Physics Group and M.A.M. is very grateful to Dr. Grahame Danby for his early efforts on this project. M.A.M. gratefully acknowledges the support of the National Science Foundation under Grant No. PHY-9408977. Finally, W.A.I. would like to thank the Department of Education for providing financial support during part of the period in which he worked on this research.

[1] Readers will find a thorough summary of theoretical work on this problem prior to 1980 in Sec. III B of N. F. Lane, Rev. Mod. Phys. **52**, 29 (1980).
[2] M. A. Morrison, Aust. J. Phys. **36**, 239 (1983).
[3] M. A. Morrison, Adv. At. Mol. Phys. **24**, 51 (1988).
[4] For a discussion of previous experimental measurements, see Sec. 4.2 of S. Trajmar, D. F. Register, and A. J. Chutjian, Phys. Rep. **97**, 220 (1983).
[5] A very thorough date compilation of e-N_2 cross sections appears in Y. Itikawa, M. Hayashi, A. Ichimura, K. Onda, K. Sakimoto, K. Takayanagi, M. Nakamura, H. Nishimura, and T. Takayanagi, J. Phys. Chem. Ref. Data **15**, 985 (1986).
[6] Y. Itikawa, Adv. At. Mol. Phys. **33**, 253 (1994).
[7] Weigo Sun and Michael A. Morrison, in *Computational Methods of Electron-Molecule Scattering Theory,* edited by W. Huo and F. Gianturco (Plenum, New York, 1995), Chap. 6.
[8] D. C. Tyte, Adv. Quantum Electron. **1**, 129 (1970).
[9] R. A. Haas, Phys. Rev. A **8**, 1017 (1973).
[10] G. J. Schulz, in *Principles of Laser Plasmas,* edited by G. Bekite (Wiley, New York, 1976), Chap. 2.
[11] A. V. Phelps, in *Electron-Molecule Scattering,* edited by S. C. Brown (Wiley-Interscience, New York, 1979), Chap. 2.
[12] G. J. Schulz, Rev. Mod. Phys. **45**, 423 (1962).
[13] B. L. Moiseiwitsch, Rep. Prog. Phys. **40**, 843 (1977).
[14] J. N. Bardsley, F. Mandl, and A. R. Wood, Chem. Phys. Lett. **1**, 359 (1967).
[15] M. Krauss and F. H. Mies, Phys. Rev. A **1**, 1592 (1970).
[16] J. G. Lauderdale, C. W. McCurdy, and A. U. Hazi, J. Chem. Phys. **79**, 2200 (1983).
[17] T. N. Rescigno, A. E. Orel, and C. W. McCurdy, J. Chem. Phys. **73**, 6347 (1980).
[18] M. Berman, O. Walter, and L. S. Cederbaum, Phys. Rev. Lett. **50**, 1979 (1983).
[19] H.-D. Meyer, Phys. Rev. A **40**, 5605 (1989).
[20] P. L. Gertitschke and W. Domcke, J. Phys. B **26**, 2927 (1993).
[21] J. N. Bardsley and F. Mandl, Rep. Prog. Phys. **31**, 471 (1962).
[22] D. T. Birtwistle and A. Herzenberg, J. Phys. B **4**, 53 (1971).
[23] L. Dubè and A. Herzenberg, Phys. Rev. A **20**, 194 (1979).
[24] A. U. Hazi, T. N. Rescigno, and M. Kurilla, Phys. Rev. A **23**, 1089 (1981).
[25] B. I. Schneider, M. Le Dourneuf, and Vo Ky Lan, Phys. Rev. Lett. **43**, 1926 (1979).
[26] M. Berman, H. Estrada, L. S. Cederbaum, and W. Domcke, Phys. Rev. A **28**, 1363 (1983).
[27] L. A. Morgan, J. Phys. B **19**, L439 (1986).
[28] C. J. Gillan, O. Nagy, P. G. Burke, L.A. Morgan, and C. J. Noble, J. Phys. B **20**, 4585 (1987).
[29] W. M. Huo, V. McKoy, M. A. P. Lima, and T. L. Gibson, in *Thermophysical Aspects of Re-entry Flows,* edited by J. N. Moss and C. D. Scott, Progress in Astronautics and Aeronautics, Vol. 103 (American Institute of Aeronautics and Astronautics, New York, 1986).
[30] W. M. Huo, T. L. Gibson, M. A. P. Lima, and V. McKoy, Phys. Rev. A **36**, 1642 (1987).
[31] J. M. Wadehra and P. J. Drallos, Phys. Rev. A **36**, 1148 (1987).
[32] J. R. Rumble, D. G. Truhlar, and M. A. Morrison, J. Phys. B **14**, L310 (1981).
[33] J. R. Rumble, D. G. Truhlar, and M. A. Morrison, J. Chem. Phys. **79**, 1846 (1983).
[34] N. Chandra and A. Temkin, Phys. Rev. A **13**, 188 (1976).
[35] C. A. Weatherford and A. Temkin, Phys. Rev. A **49**, 2580 (1994).
[36] M. A. Morrison and B. C. Saha, Phys. Rev. A **34**, 2786 (1986).
[37] G. J. Schulz, Phys. Rev. **125**, 229 (1964).
[38] H. Ehrhardt and K. Willman, Z. Phys. **204**, 462 (1967).
[39] G. J. Schulz, Phys. Rev. **135**, A998 (1973).
[40] G. C. Baldwin, Phys. Rev. A **9**, 1225 (1974).
[41] S. K. Srivastava, A. Chutjian, and S. Trajmar, J. Chem. Phys. **64**, 1340 (1976).
[42] D. E. Golden, Phys. Rev. Lett. **17**, 847 (1966).
[43] D. Mathur and J. B. Hasted, J. Phys. B **10**, L265 (1977).
[44] K. Rohr, J. Phys. B **10**, 2215 (1977).
[45] T. W. Shyn and G. R. Carignan, Phys. Rev. A **22**, 923 (1980).
[46] R. E. Kennerly, Phys. Rev. A **21**, 1876 (1980).
[47] H. Tanaka, T. Yamamoto, and T. Okada, J. Phys. B **14**, 2081 (1981).
[48] A. G. Engelhardt, A. V. Phelps, and C. G. Risk, Phys. Rev. **135**, A1556 (1964).
[49] G. Haddad, Aust. J. Phys. **37**, 487 (1984).
[50] A. V. Phelps and L. C. Pitchford, Phys. Rev. A **31**, 2932 (1985); see also JILA Data Center Report No. 26, 1985 (unpublished).
[51] O. Sueoka and S. Mori, J. Phys. Soc. Jpn. **53**, 2491 (1984).
[52] M. Allan, J. Phys. B **18**, 4511 (1985).
[53] K. Jost, P. G. F. Bisling, F. Eschen, M. Felsmann, and L. Walther, in *Abstracts of Contributed Papers, Thirteenth International Conference on the Physics of Electronic and Atomic Collisions,* edited by J. Eichler, W. Fritsch, I. V. Hertel, N. Stolterfort, and U. Wille (ICPEAC, Berlin, 1983), p. 91.
[54] W. Sohn, K.-H. Kochem, K.-M. Scheuerlein, K. Jung, and H. Ehrhardt, J. Phys. B **19**, 4017 (1986).
[55] J. Ferch, W. Raith, and A. Schweiker (private communication).
[56] M. J. Brunger, P. J. O. Teubner, A. M. Weigold, and S. J. Buckman, J. Phys. B **22**, 1443 (1989).
[57] M. J. Brennan, D. T. Alle, P. Euripides, S. J. Buckman, and M. J. Brunger, J. Phys. B **25**, 2669 (1992).
[58] X. Shi, T. M. Stephen, and P. D. Burrow, J. Phys. B **26**, 121 (1993).
[59] M. J. Brunger, S. J. Buckman, D. S. Newman, and D. T. Alle, J. Phys. B **24**, 1435 (1991).
[60] J. C. Nickel, P. W. Zetner, G. Shen, and S. Trajmar, J. Phys. Rev. E **22**, 730 (1989).
[61] M. A. Morrison, B. C. Saha, and T. L. Gibson, Phys. Rev. A **36**, 3682 (1987).

[62] R. K. Nesbet, Phys. Rev. A **20**, 58 (1979).
[63] R. J. Gulley, D. T. Alle, M. J. Brennan, M. J. Brunger, and S. J. Buckman, J. Phys. B **27**, 2593 (1994).
[64] S. J. Buckman, R. J. Gulley, M. Moghbelalhossein, and S. J. Bennett, Meas. Sci. Technol. **4**, 1143 (1993).
[65] M. J. Brunger, S. J. Buckman, and D. S. Newman, Aust. J. Phys. **43**, 665 (1990).
[66] S. J. Buckman and B. Lohmann, J. Phys. B **19**, 2547 (1986).
[67] A. Temkin and K. V. Vasavada, Phys. Rev. A **160**, 190 (1967).
[68] A. Temkin, K. V. Vasavada, E. S. Chang, and A. Silver, Phys. Rev. A **186**, 57 (1969).
[69] S. Hara, J. Phys. Soc. Jpn. **27**, 1592 (1969).
[70] E. S. Chang and U. Fano, Phys. Rev. A **6**, 173 (1972).
[71] R. J. W. Henry, Phys. Rev. A **2**, 1349 (1970).
[72] P. M. Morse, Phys. Rev. **34**, 57 (1929).
[73] K. P. Huber and G. Herzberg, *Molecular Spectra and Molecular Structure IV. Constants of Diatomic Molecules* (Van Nostrand, New York, 1979).
[74] Various conventions for normalization plane-wave and angular-momentum free states and for the relationship beween the scattering matrix and the transition matrix appear in the literature. Readers can find a guide to these conventions and the machinery for converting standard equations of scattering theory between conventions in the appendix to Ref. [7].
[75] J. R. Taylor, *An Introduction to Error Analysis* (University Science Books, Mill Valley, CA, 1982).
[76] W. N. Sams and D. J. Kouri, J. Chem. Phys. **51**, 4809 (1969).
[77] M. A. Morrison, in *Electron- and Photon-Molecule Collisions,* edited by T. N. Rescigno, B. V. McKoy, and B. I. Schneider (Plenum, New York, 1979).
[78] M. A. Morrison, N. F. Lane, and L. A. Collins, Phys. Rev. A **15**, 2186 (1977).
[79] M. A. Morrison and P. J. Hay, J. Chem. Phys. **79**, 4034 (1979).
[80] S. Huzinaga, J. Chem. Phys. **43**, 1293 (1965).
[81] T. H. Dunning, J. Chem. Phys. **55**, 3958 (1971).
[82] M. A. Morrison, Comput. Phys. Commun. **21**, 63 (1980).
[83] L. A. Collins, D. W. Norcross, and G. B. Schmid, Comput. Phys. Commun. **79**, 63 (1980).
[84] W. K. Trail, M. A. Morrison, W. A. Isaacs, and B. C. Saha, Phys. Rev. A **41**, 4868 (1990).
[85] N. J. Bridge and A. D. Buckingham, Proc. R. Soc. London Ser. A **295**, 334 (1966).
[86] J. W. Liu, G. C. Lie, and B. Liu, J. Phys. B **20**, 2853 (1987).
[87] W. K. Trail, Ph.D. thesis, University of Oklahoma, 1992 (unpublished).
[88] S. Hara, J. Phys. Soc. Jpn. **22**, 710 (1967).
[89] S. Hara, J. Phys. Soc. Jpn. **27**, 1262 (1969).
[90] M. A. Morrison and L. A. Collins, Phys. Rev. A **17**, 918 (1978).
[91] M. A. Morrison and L. A. Collins, Phys. Rev. A **25**, 1764 (1982).
[92] M. A. Morrison and L. A. Collins, Phys. Rev. A **23**, 127 (1981).
[93] T. L. Gibson and M. A. Morrison, J. Phys. B **14**, 727 (1981).
[94] M. A. Morrison, A. N. Feldt, and D. A. Austin, Phys. Rev. A **29**, 2518 (1984).
[95] W. Sun, M. A. Morrison, G. Danby, and W. K. Trail (unpublished).
[96] N. F. Lane and R. J. W. Henry, Phys. Rev. A **173**, 183 (1968).
[97] T. L. Gibson and M. A. Morrison, J. Phys. B **15**, L221 (1982).
[98] T. L. Gibson and M. A. Morrison, Phys. Rev. A **29**, 2497 (1984).
[99] A. C. Newell and R. C. Baird, J. Appl. Phys. **36**, 3751 (1965).
[100] R. H. Orcutt and R. H. Cole, J. Chem. Phys. **46**, 697 (1967).
[101] T. M. Miller and B. Bederson, Adv. At. Mol. Phys. **13**, 1 (1978).
[102] S. R. Langhoff, C. W. Bauschlicher, Jr., and D. P. Chong, J. Chem. Phys. **78**, 5287 (1983).
[103] D. Spelsberg and W. Meyer, J. Chem. Phys. **101**, 1282 (1984).
[104] M. A. Morrison and W. K. Trail, Phys. Rev. A **48**, 2874 (1993).
[105] A. Temkin, Phys. Rev. **107**, 1004 (1957).
[106] B. I. Schneider, Phys. Rev. A **74**, 1923 (1976).
[107] W. K. Trail and M. A. Morrison (unpublished).
[108] J. F. Williams, J. Phys. B **12**, 265 (1979); N. C. Steph, L. McDonald, and D. E. Golden, *ibid.* **12**, 1507 (1979); L. J. Allen, Phys. Rev. A **34**, 2706 (1986); L. J. Allen and I. E. McCarthy, *ibid.* **36**, 2570 (1987). For a review, see B. H. Bransden, in *Electron and Photon Interaction with Atoms,* edited by H. Kleinpoppen and M. R. C. McDowell (Plenum, New York, 1976), p. 161.
[109] For an application of phase-shift analysis via the spherical (central-potential) equation to e-H_2 scattering, see D. F. Register, S. Trajmar, and S. K. Srivastava, Phys. Rev. A **21**, 1134 (1988).
[110] W. A. Isaacs, W. K. Trail, and M. A. Morrison (unpublished).
[111] R. W. Crompton and M. A. Morrison, Aust. J. Phys. **46**, 203 (1993).
[112] W. H. Press, B. P. Flannery, S. A. Teukolsky, and W. T. Vetterling, *Numerical Recipes: The Art of Scientific Computing,* 2nd ed. (Cambridge University Press, New York, 1992).